UNIVERSIDAD POLITÉCNICA DE MADRID

ESCUELA TÉCNICA SUPERIOR
DE INGENIEROS DE TELECOMUNICACIÓN

MASTER OF SCIENCE IN SIGNAL THEORY AND COMMUNICATIONS

MASTER´S THESIS

ANALYSIS AND DESIGN OF A FILTER IN HIGH-TEMPERATURE SUPERCONDUCTOR TECHNOLOGY

GONZALO GARCÍA AMORÓS

2025

MASTER OF SCIENCE IN SIGNAL THEORY AND COMMUNICATIONS

MASTER´S THESIS

Title:	Analysis and design of a filter in high-temperature superconductor technology
Author:	Gonzalo García Amorós
Academic Supervisor:	Jorge Alfonso Ruiz Cruz
Department:	Señales, Sistemas y Radiocomunicaciones

MEMBERS OF THE EXAMINATION COMMITTEE

President:	……
Member:	……
Secretary:	……
Substitute:	……

The above-named members of the panel agree to grant the qualification of: ……

Madrid, … …… 2025

UNIVERSIDAD POLITÉCNICA DE MADRID

ESCUELA TÉCNICA SUPERIOR
DE INGENIEROS DE TELECOMUNICACIÓN

MASTER OF SCIENCE IN SIGNAL THEORY AND COMMUNICATIONS

RADIOFREQUENCY TECHNOLOGIES AND SYSTEMS TRACK

MASTER´S THESIS

ANALYSIS AND DESIGN OF A FILTER IN HIGH-TEMPERATURE SUPERCONDUCTOR TECHNOLOGY

DEPARTMENT OF SIGNALS, SYSTEMS AND RADIOCOMMUNICATIONS

AUTHOR

GONZALO GARCÍA AMORÓS

SUPERVISOR

JORGE ALFONSO RUIZ CRUZ

Summary

Ultra-wideband (UWB) technologies represent a significant advancement in modern communications systems, as they enable the transmission of higher data rates with high accuracy, low interference and reduced energy consumption. This has great relevance in various applications, such as medicine, radioastronomy and the military sector. These systems require low-loss radiofrequency filters capable of properly defining the operational bandwidth, for which high-temperature superconductor (HTS) materials are utilized due to their exceptional performance.

Therefore, the primary objective of this project is the study, design, and comparison of several filters with different topologies using these materials, whose frequency responses meet the requirements of ultra-wideband communications. Additionally, the project aims to analyze the impact of HTS technology through the fabrication of two designs using conventional materials, chosen due to their availability and the manufacturing complexity of HTS, and their subsequent comparison with the results obtained when employing high-temperature superconductors.

In the first stage of the project, a filter with cascaded stages and a composite filter have been designed, based on the development of an eight-order stepped impedance lowpass filter and a highpass filter with two parallel short-circuited stubs, all implemented with HTS technology. In this stage, an analysis and improvement attempt have been made on a filter sourced from the literature, which exhibits an excellent frequency response and whose study has provided several concepts and advanced design techniques.

On the other hand, the first fabricated prototype is a triple-mode stepped impedance resonator (SIR) ultra-wideband filter, centered at $f_0 = 4.35\ GHz$ and with a fractional bandwidth of $BW_{\%} = 62\%$. By the modification of the impedance ratio of the resonator and introducing parallel-coupled lines at the input and output ports, an ultra-wideband behaviour has been achieved.

The second implemented filter is an eight-pole Chebyshev ultra-wideband filter with two triple-mode stepped impedance resonators. Its design has been derived from the normalized low-pass prototype, which has been frequency-transformed, and the required parameters have been calculated to obtain a structure with two parallel-coupled SIRs whose frequency response corresponds to that of a Chebyshev filter with a return loss level of 15 dB in the passband. The filter is centered at $f_0 = 5.1\ GHz$ and has a fractional bandwidth of $BW_{\%} = 76\%$.

For both main designs, MATLAB has been used to obtain the parameters resulting from the synthesis process. Subsequently, the Advanced Design System (ADS) software has been used to simulate the circuit models with ideal and real transmission lines, adjusting to the limitations of the available technology. Electromagnetic simulations have been performed using Ansys HFSS, and MATLAB scripts have been developed to automate and accelerate this process. Finally, the prototypes have been fabricated and measured with a Vector Network Analyzer (VNA).

All these, together with the necessary theoretical foundations, are detailed across the different chapters of this document, which also include a study on efficiency and results accuracy, as well as an analysis of the social, economic, ethical and environmental impact of the project.

Keywords

Accuracy, ADS, Automation, Cascaded, Chebyshev, Compact, Composite, Coupling, Electromagnetic, Filter, HFSS, Insertion loss, Low-loss, MATLAB, Microstrip, Multi-mode, Optimization, Passband, Planar technology, Radioelectric spectrum, Return loss, Selectivity, Spurious, Stepped impedance, Stopband, Superconductor, Synthesis, Ultra-wideband.

Resumen

Las comunicaciones de banda ultra ancha (UWB) representan un gran avance en los sistemas de comunicaciones actuales, permitiendo transmitir mayores tasas de datos con alta precisión, baja interferencia y menor coste energético. Esto tiene gran importancia en diversas aplicaciones como la medicina, la radioastronomía o el ámbito militar. Estos sistemas requieren de filtros radioeléctricos de bajas pérdidas capaces de definir debidamente el ancho de banda operacional, para lo cual se utilizan materiales superconductores de alta temperatura (HTS) debido a sus excelentes prestaciones.

Por ello, el objetivo principal del proyecto es el estudio, diseño y comparación de varios filtros con distintas topologías empleando estos materiales, cuyas respuestas cumplan con los requisitos de las comunicaciones UWB. Además, se pretende analizar el impacto de la tecnología HTS mediante la fabricación de dos diseños realizados con materiales convencionales, elegidos debido a su disponibilidad y a la complejidad de los HTS, y la posterior comparación de los resultados obtenidos con cada tecnología.

En la primera etapa del proyecto se han diseñado un prototipo con etapas de filtrado conectadas en cascada y un filtro combinado a partir del desarrollo de un filtro paso bajo de salto de impedancias de orden ocho y un filtro paso alto con dos stubs paralelos terminados en cortocircuito, todo con tecnología HTS. En esta etapa además se ha analizado e intentado mejorar un filtro obtenido de la literatura del que se extraen múltiples conceptos y técnicas de diseño.

Por otro lado, el primero de los diseños principales es un filtro de banda ultra ancha con un resonador de impedancia escalonada de triple modo, centrado en $4.35\ GHz$ y con un ancho de banda porcentual del 62%. Modificado la relación entre impedancias del resonador e introduciendo líneas acopladas en paralelo en los puertos se ha conseguido un comportamiento UWB.

El segundo filtro es un filtro de orden ocho con dos resonadores de impedancia escalonada de triple modo centrado en $5.1\ GHz$ y con un ancho de banda porcentual del 76%. En su diseño se ha partido del prototipo paso bajo normalizado, se ha transformado en frecuencia y se han calculado los parámetros necesarios para obtener una estructura con dos resonadores de impedancia escalonada acoplados en paralelo con una respuesta de Chebyshev y unas pérdidas de retorno de $15\ dB$ en la banda de paso.

En ambos diseños se ha utilizado MATLAB para obtener los parámetros del proceso de síntesis. Posteriormente, se ha utilizado el Advanced Design System (ADS) para simular los modelos circuitales y ajustarse a las limitaciones de la tecnología disponible. Para la simulación electromagnética se ha utilizado el Ansys HFSS, y se han desarrollado scripts de MATLAB para automatizar y acelerar este proceso. Finalmente, se han fabricado y medido con un analizador vectorial de redes (VNA).

Todo esto, junto con los fundamentos teóricos necesarios, se recoge en los distintos capítulos de este documento, además de un estudio de eficiencia y precisión de resultados y de un análisis del impacto del proyecto en los ámbitos social, económico, ético y medioambiental.

Palabras Clave

Acoplamiento, ADS, Automatización, Banda de paso, Banda de rechazo, Banda ultra ancha, Bajas pérdidas, Cascada, Chebyshev, Compacto, Compuesto, Electromagnético, Espurio, Espectro radioeléctrico, Filtro, HFSS, Impedancia escalonada, MATLAB, Microstrip, Multimodo, Optimización, Pérdidas de inserción, Pérdidas de retorno, Precisión, Selectividad, Síntesis, Superconductor, Tecnología planar.

Acknowledgements

A mi tutor, Jorge Ruiz, por el tiempo y esfuerzo dedicados en el desarrollo de este proyecto, por su guía e interés en mi aprendizaje, por la confianza depositada en mí y por transmitirme no solo conocimientos, sino también motivación y entusiasmo por seguir aprendiendo.

A Pablo Sánchez Olivares, a José Roldán, a Gerardo y a Juan Diego, por su generosa ayuda, únicamente con el propósito de hacer posible la fabricación y medida de los diseños de este proyecto.

A José Ramón, por su dedicación e interés hacia mi formación y crecimiento, y por los consejos y la orientación que me han acompañado y me acompañarán tanto en el ámbito académico como en el mundo profesional.

Contents

List of figures

List of tables

Glossary

ADS	–	Advanced Design System
CAD	–	Computer Aided Design
COM	–	Component Object Model
EM	–	Electromagnetic
FEM	–	Finite Element Method
HFSS	–	High Frequency Structure
HPF	–	Highpass Filter
HTS	–	High-Temperature
I/O	–	Input/Output
IL	–	Insertion Loss
LPF	–	Lowpass Filter
MMR	–	Multiple Mode Resonator
OLE	–	Object Linking and Embedding
PLD	–	Pulsed Laser Deposition
RL	–	Return Loss
SIR	–	Stepped Impedance Resonator
UIR	–	Uniform Impedance Resonator
UWB	–	Ultra-Wideband
VBA	–	Visual Basic
VLBI	–	Very Long Baseline
VNA	–	Vector Network Analyzer
YBCO	–	Yttrium Barium Copper Oxide

CHAPTER ONE

Introduction

1.1. OVERVIEW

Modern society increasingly relies on wireless communication systems. Mobile phones, teleworking, industrial automation and smart cities are clear examples, among many others, of the exponential growth of connected devices. This has turned the radioelectric spectrum a critical yet limited resource. Efficient spectrum management is essential to ensure the correct functioning of all systems, guarantee signal integrity, and minimize interference. In this context, radiofrequency filters have a fundamental role since they are responsible for selecting the desired frequency bands and rejecting unwanted signals, optimizing the radioelectric spectrum.

The evolution of mobile communications technology also entails a growing demand for higher data rates and low energy consumption. In this context, ultra-wideband (UWB) wireless communications have emerged as a compelling option. They are characterized by transmitting data in form of short pulses over an extremely wide frequency range. According to the corresponding regulations, their frequency range is from 3.1 GHz to 10.6 GHz, as depicted in Figure 1.1, and their power spectral density is limited to -41.3 dBm/MHz, enabling high data transmission rates with relatively low power usage [1]. Nevertheless, in certain specialized applications, these parameters are adjusted to comply with specific operational requirements [2].

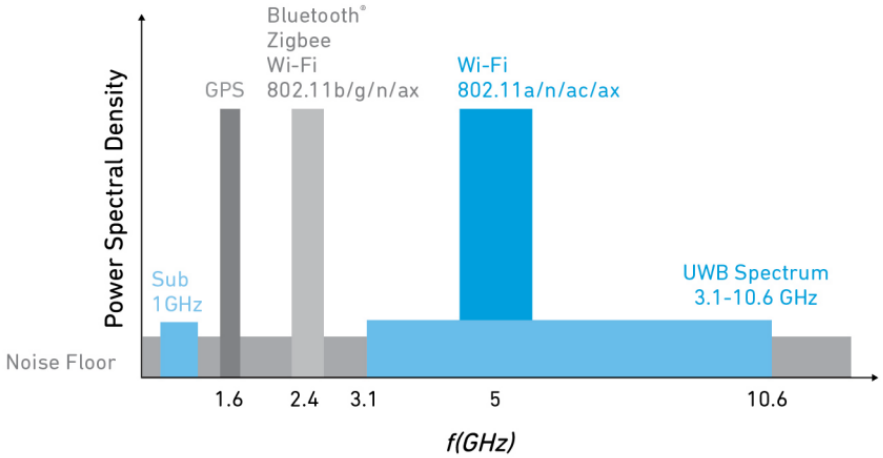

Figure 1.1. Frequency Spectrum Coverage of UWB and General Communication Bands [3].

The short pulses make it possible to precisely determine the instant in which the signal is transmitted and received, generating a higher temporal resolution, which translates into the ability to distinguish distances with high accuracy. These has overhauled localization systems in multiple sectors such as the automotive industry, consumer electronics or radar tracking.

Medical field has also benefited from the advantages of ultra-wideband technology, not only in patient monitoring, but also in medical imaging. Due to its ability to transmit high-precision, low-interference signals, as well as its low energy consumption, UWB systems can penetrate human tissues, capturing detailed images without the need for invasive methods. This makes it a key technology in the early detection of diseases such as tumours or cardiac anomalies [4].

Another field in which ultra-wideband systems represent a significant advancement is radio astronomy. In the realm of radio astronomy, UWB technology enables capturing weak signals in a wide range of frequencies and enhancing the sensitivity and accuracy of receivers, allowing the detection of cosmic phenomena such as pulsars, quasars, and cosmic microwave background radiation. Additionally, in very long baseline interferometry (VLBI) networks, UWB ensures precise synchronization between geographically distributing antennas, enabling extremely high angular resolution [5] [6].

The correct functioning of the systems in all these applications depend on the use of high-quality, low-loss filters capable of sharply defining the operational bandwidth. Traditional filter technologies often struggle to meet the stringent requirements of compactness, high selectivity and low insertion loss of UWB systems.

To address these challenges, the use of high-temperature superconducting (HTS) filters has become an excellent solution. These microstrip filters employ HTS thin films instead of traditional conductor films, offering exceptional electromagnetic performance in terms of selectivity and passband insertion loss. They present unique properties at cryogenic temperatures, such as extremely low resistance and minimal energy loss, which makes HTS filters particularly suitable in many of the above-mentioned applications with such stringent requirements [7].

1.2. OBJECTIVES

The primary objective of this project is to conduct a thorough investigation and a comprehensive understanding of the analysis and design of filters in high-temperature superconducting technology (HTS), with particular emphasis on ultra-wideband applications. The study aims to explore sophisticated techniques applied in such designs, with the intention of subsequently implementing them to original filter designs.

To achieve this, an extensive review of existing designs documented in the literature will be undertaken, starting with the theoretical foundations and progressing through the stages of design and implementation. Additionally, a final design will be developed using the available manufacturing technology, different from HTS, whose results will serve as a basis for comparison with those achieved using high-temperature superconducting technology.

Furthermore, given the inherent complexity of these filters and their reliance on computer-aided processes, this project will include a detailed assessment of analytical software, automation strategies, result accuracy, and electromagnetic optimization approaches. As a secondary yet significant objective, this endeavour aims to enhance the efficiency of the design process and ensuring the attainment of highly reliable and accurate results.

CHAPTER TWO

Overview of Filter Design: Brief Summary of Principles, Techniques, and Technologies

2.1. FUNDAMENTALS OF FILTER DESIGN

A filter is a linear, passive, causal, and ideally lossless device. It allows the signal to pass within a certain frequency range, known as passband, and blocks it in another range, called stopband [8]. They are highly important components in communication systems since they enable efficient use of electromagnetic spectrum, which is a limited and costly resource.

Filters can be classified into different groups depending on the type of response: low-pass, high-pass, band-pass, band-stop, and all-pass. This is represented in Figure 2.1.

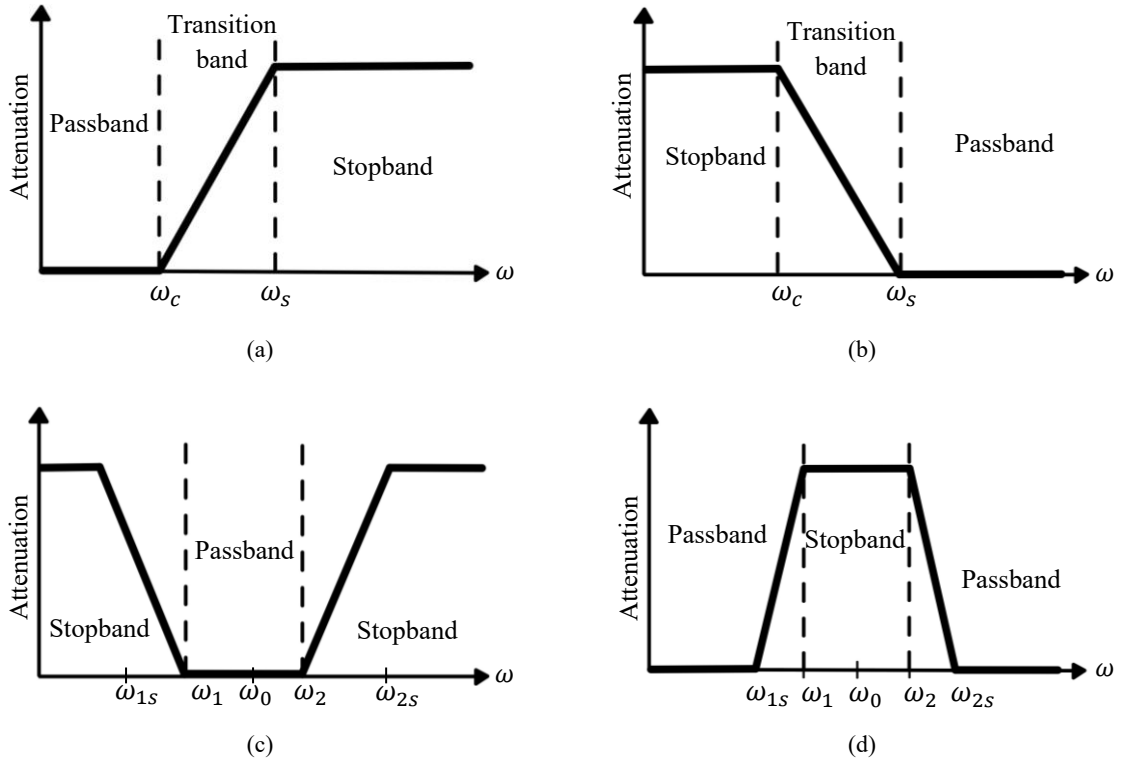

Figure 2.1 Classification of filters: (a) low-pass, (b) high-pass, (c) band-pass, (d) band-stop. Source: [8].

2.1.1. Transfer Function

The network response of a two-port filter can be expressed by an amplitude-squared transfer function, which relates the available power from the generator (P_{ag}) to the dissipated power in the load (P_L):

$$|H(j\omega)|^2 = \frac{P_L}{P_{ag}} \tag{2.1}$$

where

$$H(j\omega) = R(\omega) + jX(\omega) = |H(j\omega)|e^{j\theta(\omega)} \tag{2.2}$$

is the transfer function of the filter.

In filter design, scattering parameters (S-parameters) are commonly employed. Consequently, it is convenient to express (2.1) as:

$$|H(j\omega)|(dB) = 20\,log_{10}|s_{21}| \tag{2.3}$$

This expression can be used when the load impedance (R_L) and the generator impedance (R_g) are equal. This requirement will be satisfied throughout the project, since $R_L = R_g = 50\Omega$ is used by default.

The schematic of a generic filter is represented in Figure 2.2.

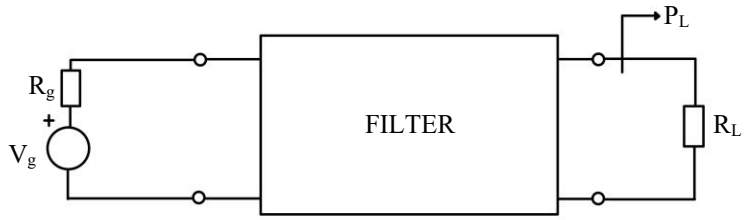

Figure 2.2 Schematic of a generic filter.

2.1.2. Insertion Loss. Return Loss

Insertion Loss (IL) of a two-port filter is defined as the ratio between the power delivered to the load when the filter is not connected and the power delivered in the presence of the filter [8].

It is also important to define the Return Loss (RL), which is directly related to the reflection coefficient at the input of the filter.

Again, considering that identical generator and load impedances will be used, it is convenient to express these parameters in terms of the scattering parameters:

$$IL(dB) = -20\log_{10}|s_{21}| \tag{2.4}$$

$$RL(dB) = -20\log_{10}|s_{11}| \tag{2.5}$$

2.1.3. Group Delay

Another fundamental parameter in filter design is the group delay. It is defined as the delay experienced by the signal components within the system as a function of frequency, and it can be computed as the negative first derivative of the phase of the filter's transfer function with respect to frequency [9]:

$$D_l(\omega) = -\frac{d\theta(\omega)}{d\omega} \tag{2.6}$$

The greater the variation in group delay within the passband, the larger the difference in delay experienced by different frequency components, which leads to signal distortion. Therefore, it is desirable for the group delay to be maximally flat within the band of interest.

2.1.4. Quality Factor

In a resonant circuit, the quality factor (Q) is the parameter that measures the losses of the circuit, and it is expressed as [10]

$$Q = \omega \frac{W_m + W_e}{P_{loss}} \tag{2.7}$$

where $\omega = 2\pi f$ is the angular frequency and W_m and W_e are the average magnetic and electric energies stored in the inductor and the capacitor, respectively, of the RLC lumped-element equivalent circuit [10].

The quality factor of an isolated resonator, without considering external effects, is referred to as unloaded Q, or Q_0. This parameter quantifies the ratio between the stored energy and the energy lost due to dielectric losses, radiation or conductive losses. Its expression is given by

$$Q_0 = \begin{cases} \dfrac{1}{\omega_0 RC} & for\ series\ resonant\ circuits \\ \omega_0 RC & for\ parallel\ resonant\ circuits \end{cases} \tag{2.8}$$

where ω_0 is the resonant frequency.

However, resonators are usually connected to external circuits that introduce additional effects. For this reason, the external quality factor is defined as [10]

$$Q_e = \begin{cases} \dfrac{\omega_0 L}{R_L} & for\ series\ circuits \\ \dfrac{R_L}{\omega_0 L} & for\ parallel\ circuits \end{cases} \tag{2.9}$$

The loaded Q or Q_L accounts for both contributions:

$$\frac{1}{Q_L} = \frac{1}{Q_e} + \frac{1}{Q_0} \tag{2.10}$$

This parameter will play a key role in the development of the two main designs of the project.

2.2. ULTRA-WIDEBAND (UWB) FILTERS

In Section 1.1 it has been presented the importance of ultra-wideband systems in modern applications, along with the necessity of efficiently managing the radioelectric spectrum to guarantee their correct functioning.

Consequently, ultra-wideband filters have emerged to select the desired signals over a wide frequency range while rejecting undesired ones.

Due to the regulations outlined in that same section regarding the frequency band of operation of UWB wireless communications, most of these filters feature a passband from 3.1 GHz to 10.6 GHz. Nevertheless, there are certain applications that require filters with a wider or different bandwidth, and each application demands specific requirements, thus giving rise to an unlimited variety of configurations and technologies in the development of such filters.

In this project, several configurations will be presented, starting from their synthesis process, considering the specific challenges associated with its implementation, and subsequently evaluating the achievable results.

2.3. HIGH-TEMPERATURE SUPERCONDUCTING (HTS) FILTERS

Superconductivity is a physical phenomenon that occurs in specific materials when they are cooled below a particular temperature, at which their electrical resistance instantly disappears, meaning the transition to a state in which an electric current can flow through the material without any energy loss. The temperature at which this transition from the material's standard state to the superconducting state occurs is referred to as the critical temperature T_c [11].

This phenomenon was discovered in 1911. Initially, all known superconductors had a very low critical temperature, lower than 30K. The difficulty of cooling them to such temperatures severely limited their practical use. It was not until 1986, that superconductors with a critical temperature above 77K were discovered. This advancement allowed the use of liquid nitrogen as a cooling medium, as its boiling point corresponds to this temperature, enabling their use in many practical applications [7] [11]. For this reason, such materials are known as high-temperature superconductors (HTS).

There exist many superconducting materials. One of the most widely used, and the basis for this project, is yttrium barium copper oxide (YBCO). Its chemical formulation is $YBa_2Cu_3O_{7-\delta}$, where the subindex in the oxygen indicates a variable content, typically close to seven [12].

HTS materials are usually fabricated in thin films (typically $500\ nm$ to $1\ \mu m$), which are deposited on dielectric substrates using methods such as pulsed laser deposition (PLD) or sputter techniques, among others. The selection of the substrate material is critical, as it must provide good structural compatibility with the superconductor. This includes having similar thermal expansion coefficient and avoiding any chemical interaction at the interface between HTS and substrate, besides other considerations [12].

For microwave applications, it is essential for the substrate to have a low loss tangent ($tan\delta < 10^{-5}$) to preserve the advantages of using a superconductor. For this reason, and due to its compliance with the aforementioned considerations, magnesium oxide (MgO) is a suitable choice and one of the most commonly used in practice for YBCO deposition [12]. Table 2.1 shows its properties.

As has been evidenced, HTS materials exhibit unique electromagnetic properties which, when integrated with appropriately selected dielectric materials, have enabled the development of highly efficient microwave filters.

ε_r	$tan\delta$ at 10 GHz, 77K	Thermal expansion coefficient $(10^{-6}/°C)$
9.6-10	$6.2 \cdot 10^{-6}$	*14*

Source: QIU, X., 2011. High-temperature superconductors. 1st edition. S.l.: s.n. ISBN 9780857091031.

Table 2.1: MgO dielectric properties.

The main advantages of high-temperature superconducting filters lie in their exceptionally low energy losses, high selectivity, and compact size. Owing to the negligible surface resistance of superconductors, these filters exhibit minimal attenuation in the passband and significantly high-quality factors, which allows sharply defining the operational bandwidth. Furthermore, the use of high-permittivity dielectric substrates allows for remarkable miniaturization, making the HTS filters ideal for situations where high performance and compactness are required.

The benefits of this technology have driven progress in many other fields, such as radio astronomy, where receivers are cooled to temperatures around 20K, at which HTS filters provide excellent performance [7].

Leveraging these advantages, research has increasingly focused on ultra-wideband (UWB) HTS filters, aiming to extend the benefits of superconducting technology to wider frequency ranges, as explained in the previous section. The design of these filters presents significant challenges, as wide bandwidths usually compromise selectivity, quality factor, and size. However, by exploiting advanced resonator topologies and carefully optimizing designs, it is possible to achieve high-performance UWB filters based on high-temperature superconductors that maintain low insertion losses and compactness.

CHAPTER THREE

Overview of Computer-Aided Design (CAD): Brief Summary of the Analysis Tools and Optimization Techniques Applied in the Project

3.1. OPTIMIZATION PROCEDURES

The designs analyzed and developed in this project are all based on various synthesis processes, from which the necessary parameters for the implementation of each filter are derived. However, these processes involve approximate calculations, leading to non-ideal results. Moreover, many of the studied topologies include couplings and discontinuities that degrade the filter's response. Therefore, once the initial response is obtained, it is often necessary to optimize the filter parameters to align the response more closely with the desired performance.

In simpler cases, circuit-level optimization is sufficient to achieve the expected outcome, whereas in others, electromagnetic optimization of the structure is also required.

The optimization processes involve minimizing a performance criterion, expressed as a scalar measure of the difference between existing and desired response [13]. This is subject to a set of specifications defined based on the problem and the intended objective, which may include lower and upper bounds on the variable to be optimized. Such constraints are particularly useful when designs are size-limited.

The function to be minimized, commonly referred to as the cost function, usually involves the magnitude of scattering parameters, group delays, and similar metrics. In this project, the specifications are built by requirements on minimum out-of-band rejection and maximum attenuation in the passband. These specifications can be assigned different weights based on their relative importance. It is crucial to accurately define the cost function and appropriately assign the weights to achieve optimal results.

A common definition of the cost function, which is the one used in this project, is the following [14]:

$$\begin{aligned} Passband: \quad & U_p(j) = \left| \frac{S_{11_{spec}}(j)}{S_{11_{simul}}(j)} \right|, \quad j = 1, 2, \dots, N_p \\ Stopband: \quad & U_s(j) = \left| \frac{S_{21_{spec}}(j)}{S_{21_{simul}}(j)} \right|, \quad j = 1, 2, \dots, N_s \end{aligned} \tag{3.1}$$

where $S_{11_{simul}}$ and $S_{21_{simul}}$ denote the simulated scattering parameters, and $S_{11_{spec}}$ and $S_{21_{spec}}$ the specified or desired S-parameters. The index j represents the sampling frequency points, while N_p and N_s correspond to the number of discrete frequency points considered in the passband and stopband, respectively. Accordingly, the objective function to be minimized is defined as

$$U = W_1 \cdot \sum_{j=1}^{N_p} U_p^2(j) + W_2 \cdot \sum_{j=1}^{N_s} U_s^2(j) \tag{3.2}$$

being W_1 and W_2 the corresponding weighting factors.

Currently, EM simulators such as CST Studio Suite, Ansys HFSS, and Momentum Microwave include powerful optimization tools that greatly facilitate this process. Nevertheless, electromagnetic optimization involves high computational cost, so it must be considered when defining the number of frequency points and the mesh refinement of the simulation, among other things.

In this project, both self-defined optimization procedures and the optimization tools of the aforementioned softwares will be employed. In the first case, simulation variables will be extracted and MATLAB's Optimization Toolbox, along with its different functions and algorithms, will be used to minimize the defined cost functions. This approach provides greater control over the optimization process. In the latter case, explicit goals will be established based on the specifications of each design, and the corresponding weighting factors will be assigned, carefully adjusting the parameters provided by each tool.

3.2. AUTOMATION

The need for electromagnetic optimization of designs requires a large number of iterations of the structure with variations on the corresponding design variables. This, in turn, means obtaining multiple simulation responses and values of the variables that must be collected and analyzed to ensure the correct functioning of the algorithm. In the case of the optimization tools of electromagnetic simulators, this process is practically invisible to the user. However, in self-defined processes, it can become a tedious and time-consuming task.

Furthermore, given that the design variables change in each iteration and therefore the structure varies in size, it is strictly necessary for the structure to be properly parametrized. Otherwise, the optimization process might fail dramatically.

This makes it necessary to implement automation techniques during the process. In this project, for the optimization carried out in MATLAB as described earlier, automation scripts have been developed to accelerate the design and simulation process of the filters made using Ansys HFSS software. In the available literature, some examples of automation scripts using Python through Visual Basic (VBA) have been found. However, this project utilizes scripts that control HFSS through an ActiveX/COM interface.

COM (Component Object Model) is a Microsoft technology that allows different applications to communicate between them through objects. On the other hand, ActiveX is a specific implementation of COM for applications with graphic interfaces, which allows the integration and automation of Windows applications [15]. The used interface creates a local OLE (Object Linking and Embedding) automation server, a mechanism that allows creating and editing documents containing elements or objects that have been created by various applications [16].

In this case, MATLAB acts as a COM client and HFSS as a COM server, meaning that HFSS object can be created, controlled and manipulated in MATLAB as they were functions of this tool itself.

Specifically, in this project, the interface is used to define the design variables, generate the structure to be simulated, define the ports and simulation region, configure the analysis setup and frequency sweep settings and, after the simulation, extract the obtained S-parameters to MATLAB in order to analyze them.

This significantly streamlines the optimization process within MATLAB, as it is only necessary to select the optimization algorithm, define the cost function as explained in Section 3.1, and update the design variables at each iteration in the simulation software.

These developed scripts, in addition to being used to optimize designs, are also employed throughout the project to automatically generate structures in HFSS directly from MATLAB, which is particularly useful as it enables the same code to be reused by modifying and adding only the definitions of the specific elements of each design, thereby accelerating the creation of new geometries.

Some examples of the automation scripts are shown in Figures 3.1, 3.2 and 3.3.

```
% ----------------------------  CREATE ActiveX server
try
    app = actxserver('Ansoft.ElectronicsDesktop');

    oDesktop = app.GetAppDesktop();

    oDesktop.RestoreWindow;

    oDesktop.NewProject;

    oProject = oDesktop.GetActiveProject ;

    oProject.InsertDesign("HFSS", "HFSSDesign1", "HFSS Terminal Network", "");

    oDesign = oProject.SetActiveDesign("HFSSDesign1") ;

    oEditor = oDesign.SetActiveEditor("3D Modeler") ;

    oDefinitionManager = oProject.GetDefinitionManager();

    oModule = oDesign.GetModule("BoundarySetup");

catch ME
    disp('An error occurred while trying to open Electronics Desktop:');
    disp(ME.message);
end
```

Figure 3.1. Automation scripts in MATLAB. Creation of ActiveX server.

```
% ----------------------------  ADD MATERIAL ----------------------------
oDefinitionManager.AddMaterial(...
    {
        "NAME:MgO",...
        "CoordinateSystemType:=", "Cartesian",...
        "BulkOrSurfaceType:="   , 1,...
        {...
            "NAME:PhysicsTypes",...
            "set:="         , "Electromagnetic"...
        },...
        "permittivity:="    , "9.6"...
        "dielectric_loss_tangent:=", "0"...
    })
```

Figure 3.2. Automation scripts in MATLAB. Add material.

```
% ----------------------------  SUBSTRATE --------------------------------
XPos_subs = -l_subs/2;          % Origin point (X-axis)
YPos_subs = -w_subs/2;          % Origin point (Y-axis)
ZPos_subs = -h_subs;            % Origin point (Z-axis)

XPos_subs_string = [num2str(XPos_subs) 'mm'];    % |
YPos_subs_string = [num2str(YPos_subs) 'mm'];    % |> String format for HFSS
ZPos_subs_string = [num2str(ZPos_subs) 'mm'];    % |

oEditor.CreateBox( ...
    { ...
        "NAME:BoxParameters", ...
        "XPosition:=", XPos_subs_string, ...
        "YPosition:=", YPos_subs_string, ...
        "ZPosition:=", ZPos_subs_string,...
        "XSize:=",     l_subs_string, ...
        "YSize:=",     w_subs_string, ...
        "ZSize:=",     h_subs_string ...
    }, ...
    { ...
        "NAME:Attributes", ...
        "Name:=", 'Substrate', ...
        "Flags:=", "", ...
        "Color:=", '(192 192 192)', ...
        "Transparency:=", 0, ...
        "PartCoordinateSystem:=", "Global", ...
        "UDMId:=", "", ...
        "MaterialName:=", 'MgO', ...
        "SurfaceMaterialValue:=", '""', ...
        "SolveInside:=", true, ...
        "ShellElement:=", false, ...
        "ShellElementThickness:=", '0mm', ...
        "ReferenceTemperature:=", '20cel', ...
        "IsMaterialEditable:=", true, ...
        "IsSurfaceMaterialEditable:=", true, ...
        "UseMaterialAppearance:=", false, ...
        "IsLightweight:=", false ...
    } ...
);
```

Figure 3.3. Automation scripts in MATLAB. Create substrate.

3.3. ACCURACY

In the context of advanced microstrip filter design, the accuracy of electromagnetic simulation results is an important aspect to be considered. It is influenced by several factors, including the correct definition of excitation ports during the simulation, the type of electromagnetic solution used, and the balance between precision and computational efficiency.

A study on simulation scenarios employing different excitation mechanisms, simulation region sizes, and meshing strategies has been carried out, with the objective of finding the best possible configuration in terms of time consumption and precision for each of the design cases.

3.3.1. Excitation Ports

This study incorporates two commonly employed excitation ports for planar structures: lumped ports and wave ports.

Lumped ports are typically used to feed planar transmission lines. They must be located inside the simulation boundaries, placed between the signal conductor and a ground plane. They allow the user to

obtain the scattering parameters normalized to the specified characteristic impedance by a single-mode propagation analysis.

On the other hand, wave ports are typically employed for closed structures, but they can also be used to feed printed transmission lines. They calculate the scattering parameters normalized to the computed characteristic impedance by a multiple-mode analysis. Wave ports must touch the background object, making sure that the transmission line fields do not interact with the port's boundary condition [17]. They provide more precise results than lumped ports, but they increase the design complexity because some additional considerations must be taken for its correct definition, since inappropriate port dimensions can lead to incorrect results. In particular, characteristic impedance estimation and undesired reflections are strictly related with port width, so it must be wide enough, and the height of the port is determined by the permittivity of the substrate, since low permittivity implies more field propagating in the air and therefore requires larger ports.

A visual representation of the proper definition of wave ports is presented in Figure 3.4.

Although more complex and computationally expensive, wave ports offer greater robustness for automated parametrization, making it particularly advantageous when integrated into script-driven simulations. Consequently, in this project, lumped ports are used for simple and fast simulations, and wave ports when simulating and optimizing using the aforementioned scripts.

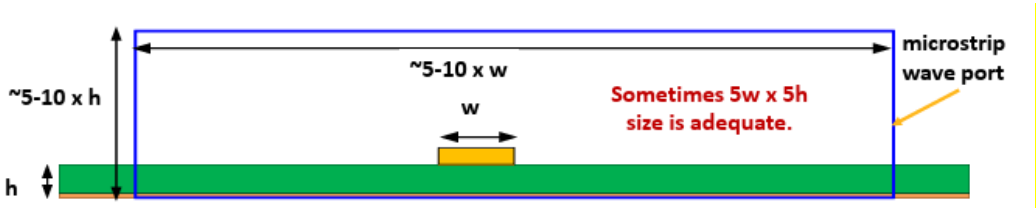

Figure 3.4. Wave port definition scheme. Source: [17].

Throughout the project, results from several designs will be presented, including both wave ports and lumped ports, allowing for a comparison and verification of the influence of each port type on the filter's response.

3.3.2. Radiation Region Size

Simulation accuracy is also affected by the radiation region, which is the outer boundary of the simulation space for open structures. Boundaries define the computational volume for the Finite Element Method (FEM) in HFSS [18].

Unlike closed models, as waveguides, which confine all energy, open models require careful management of radiation effects. Radiation boundaries allow energy to radiate outward, approximating free-space conditions through absorbing boundary conditions. Nevertheless, those boundaries must be correctly defined in order to obtain accurate results, so the size of the radiation box is a critical parameter of the simulation.

Typically, radiation boundaries are positioned a quarter wavelength ($\lambda/4$) from any radiation edge of the structure at the higher frequency of the simulation to prevent even the shortest wave from being reflected at the boundary. However, in some cases this is not enough to minimize reflections and ensure effective absorption of outgoing electromagnetic waves.

Thus, convergence studies have been conducted to optimize the size of the radiation region. Some of the filters examined throughout the project require increasing the distance to $\lambda/2$ or even $3\lambda/4$ to achieve accurate results, particularly for low-frequency behaviour analysis and wideband filter designs. Indeed, separate frequency sweeps have been occasionally performed to maintain simulation accuracy across the broad bandwidth of the proposed designs.

3.3.3. Mesh Density

Another critical factor impacting accuracy is the density of the Finite Element mesh. A finer mesh enables more precise field computations, particularly in regions with discontinuities such as coupling gaps or stepped impedance transitions. However, excessively fine meshing can significantly increase computational cost.

Although the exploration of the various possible meshing strategies is beyond the scope of this project, this aspect has been considered in all the designs. A balance between time consumption and result accuracy has been maintained by using coarser meshes during initial simulations and optimization processes, with subsequent validation of results using sufficiently refined meshes.

CHAPTER FOUR

Overview of Advanced Filter Synthesis Techniques for Ultra-Wideband (UWB) Applications

4.1. CASCADED FILTERING STAGES FOR ULTRA-WIDEBAND REALIZATION

One of the simplest techniques for designing ultra-wideband filters is a cascade connection of a lowpass filter and a highpass filter. This latter eliminates low frequencies, thus controlling the lower stopband, while the lowpass filter removes high frequencies, controlling rejection in the upper stopband [19].

By designing a lowpass filter with a sufficiently high cutoff frequency f_H and a highpass filter with a low cutoff frequency $f_L < f_H$, and connecting them directly, an ultra-wideband behaviour can be obtained.

To demonstrate this, the corresponding designs have been developed. Since the objective of this section is not the design procedure of these individual filters, but the combined performance when connected in cascade, the design details will not be discussed in depth.

First, a 9th-order Chebyshev stepped-impedance lowpass filter in microstrip technology has been designed. The filter has a cutoff frequency $f_H = 10.6\ GHz$ and a return loss (RL) of 17 dB, which establishes the design condition [9]. Additionally, a highpass filter has been designed using two parallel short-circuited stubs, with a cutoff frequency $f_L = 3.1\ GHz$ and a return loss of 17 dB [7]. Both filters have been developed by setting the minimum possible line width to $0.125mm$.

The employed substrate is magnesium oxide (MgO) with YBCO HTS thin films, whose characteristics, as explained in Section 2.3, are depicted in Figure 4.1.

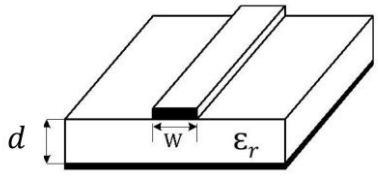

$d = 0.5\ mm$

$\varepsilon_r = 9.6$

$tan\delta = 6.2 \cdot 10^{-6}$

Figure 4.1. Microstrip line high-temperature superconducting technology. Source: [26]

As it can be deduced, the aim is to achieve a passband from 3.1 GHz to 10.6 GHz, which corresponds to the designated frequency range for ultra-wideband applications.

The individual performances of the filters after the circuit optimization using Advanced Design System (ADS) software from Keysight Technologies, as well as their layout, are presented in Figure 4.3 and Figure 4.2 respectively.

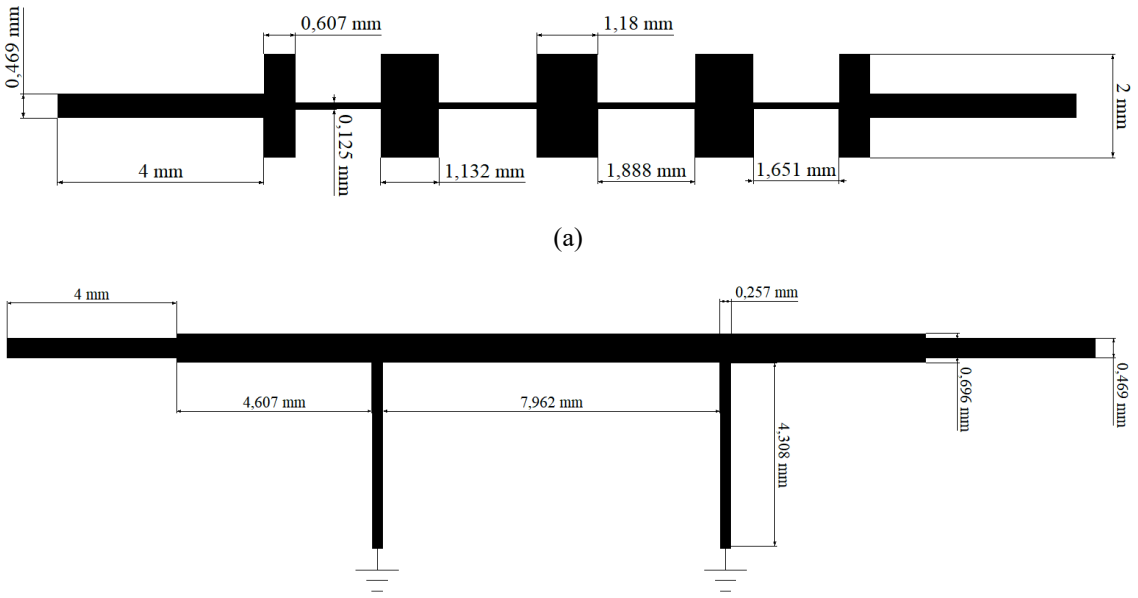

Figure 4.2. Layout of (a) 9th-order Chebyshev stepped-impedance lowpass filter and (b) highpass filter with two parallel short-circuited stubs.

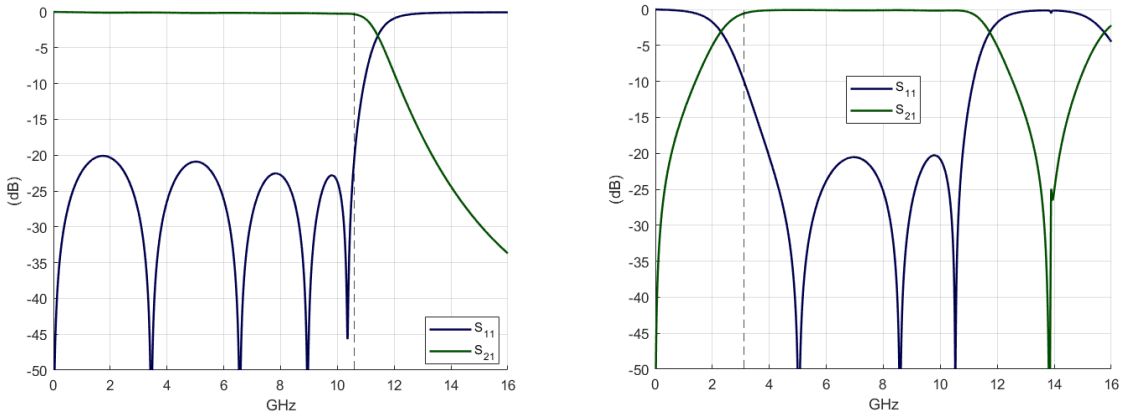

Figure 4.3. Circuit response of (a) 9th-order Chebyshev stepped-impedance lowpass filter and (b) highpass filter with two parallel short-circuited stubs.

As it can be observed, both designs meet the established requirements. Nevertheless, the highpass filter has a similar behaviour to that of a bandpass filter, which is due to the fact that transmission lines have a periodic frequency response. However, for the purpose of this case, which is to reject frequencies below 3.1 GHz and allow those above up to 10.6 GHz to pass, it can be considered a pseudo-highpass filter.

Therefore, next step is to connect both filters in cascade, as explained before. Again, this process has been carried out using ADS software.

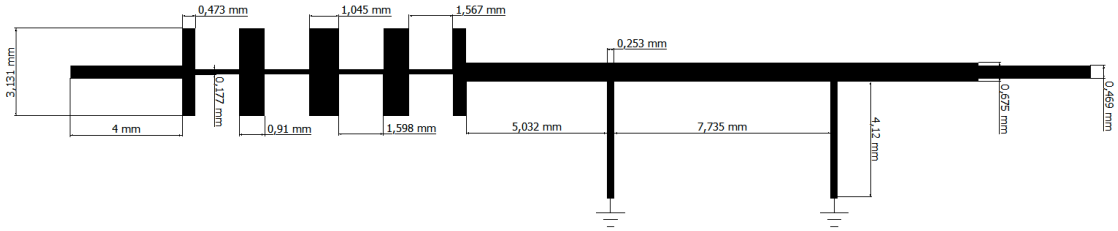

(a)

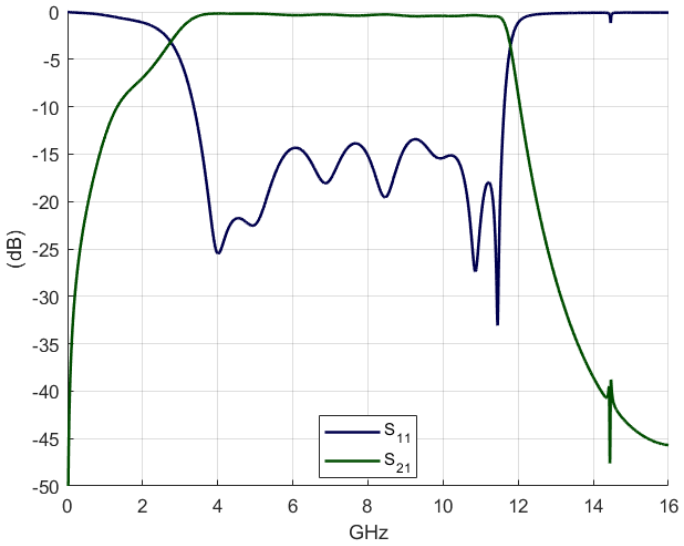

(b)

Figure 4.4. Ultra-wideband filter with cascaded filtering stages. (a) Layout and (b) Circuit response.

Figure 4.4 shows the layout and circuit response of the cascaded filtering stages after circuit optimization. The presented result exhibits an ultra-wideband behaviour, as expected. The passband goes from 3.5 GHz to 11.5 GHz, and it has been achieved a return loss better than 13 dB, along with high attenuation in the upper stopband. However, the attenuation level in the lower stopband is significantly low, likely insufficient for most UWB applications, where it is necessary to have a better rejection of signals below 3.1 GHz. This is mainly due to the simplicity of the highpass filter. Designing a more sophisticated one could possibly improve this characteristic of the filter, but it would significantly increase the total length of the structure, which is not optimal given that compactness is typically required in such designs.

Therefore, although this topology allows to obtain a relatively simple UWB filter, it is necessary to explore other methodologies to achieve a higher level of out-of-band rejection and a more compact design.

4.2. COMPOSITE FILTER DESIGN

In the previous section it has been examined how cascading a lowpass filter and a highpass filter results in an ultra-wideband filter, and also the limitations this has in terms of performance and size.

There are other similar topologies in which the direct connection of both filters is replaced by embedding the HPF and the LPF, as the one presented in [20]. This approximation provides a more compact design.

To study this technique, a structure incorporating impedance steps and parallel short-circuited stubs has been developed, based on the designs of the previous sections. After optimizing the design variables to achieve a response that meets the established requirements, a composite structure has been obtained, which is shown in Figure 4.5.

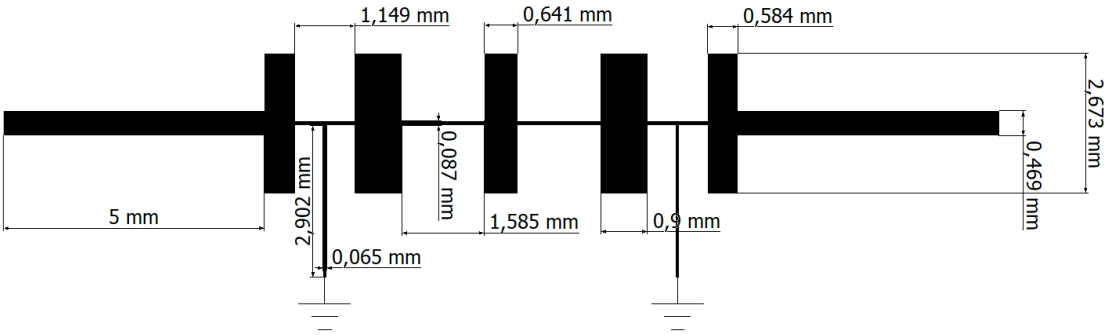

(a)

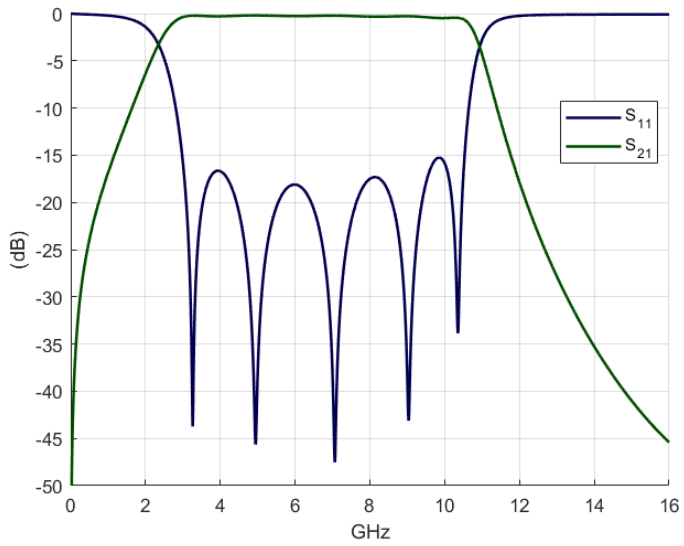

(b)

Figure 4.5. Ultra-wideband filter with embedded filtering stages. (a) Layout and (b) Circuit response.

It can be noted that an ultra-wideband filter has been achieved, with a return loss better than 15 dB across the entire passband and good attenuation in the stopband.

Figure 4.6 presents a comparison of the responses of the two studied topologies, namely embedded and cascaded configurations. It can be discerned that the second one allows for a more closely matched passband to the desired one, between 3.1 GHz and 10.6 GHz, with a flatter insertion loss level and a lower return loss level, indicating better adaptation.

Therefore, it can be concluded that the embedded topology requires a more complex design, but it achieves a better performance and a more compact design that the cascaded solution.

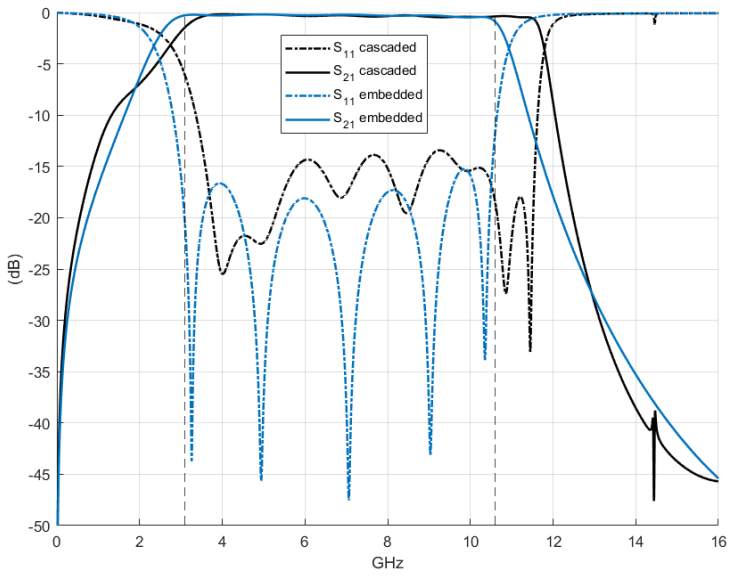

Figure 4.6. Ultra-wideband filter with cascaded filtering stages vs. embedded filtering stages. Circuit responses.

To verify the proper performance of the ultra-wideband filter with embedded filtering stages, an electromagnetic study of the structure has been conducted. For this purpose, Ansys HFSS software has been used.

Through the parametrization scripts in MATLAB presented in Section 3.2, and after the corresponding convergence and results accuracy study, the electromagnetic response of the structure has been obtained, as depicted in Figure 4.7. It presents the simulation results obtained with the two types of excitation ports under study, lumped port and wave port. In both cases, the radiation region size has been modified ensuring the absence of reflections and undesired effects, and an adaptive meshing process with 13 refinement steps has been employed.

It can be observed that both electromagnetic simulation results are similar to each other and do not deviate significantly from the circuit response.

Figure 4.8 shows the group delay and power balance of the filter. It can be observed that the delay variation in the passband is lower than 0.25 ns. On the other hand, losses remain below 9% of the total power over the entire band of interest, which is mainly due to the use of a HTS material with very low loss tangent, and a high-permittivity dielectric, allowing for more compact designs with lower radiation losses, which would be considerably higher if a conventional substrate were used.

The requirement to drill the substrate in order to realize a short circuit in microstrip technology considerably increases the complexity of the manufacturing process of this structure, thus limiting its study to the electromagnetic simulation phase. Nevertheless, it can be concluded that this topology yields highly favourable results for the design of UWB filters in this technology.

Moreover, the results obtained in this section could be improved through a more refined design of the highpass stage and a subsequent electromagnetic optimization of the entire structure. However, fabrication constraints regarding minimum dimensions of the transmission lines should be considered.

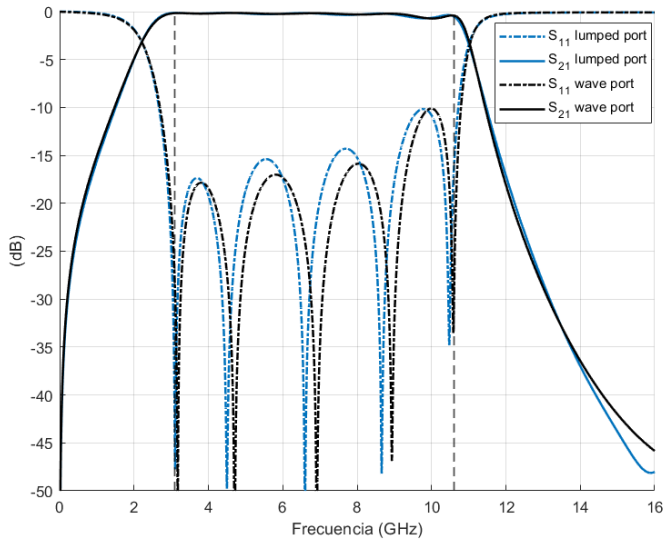

Figure 4.7. Ultra-wideband filter with embedded filtering stages. Electromagnetic response.

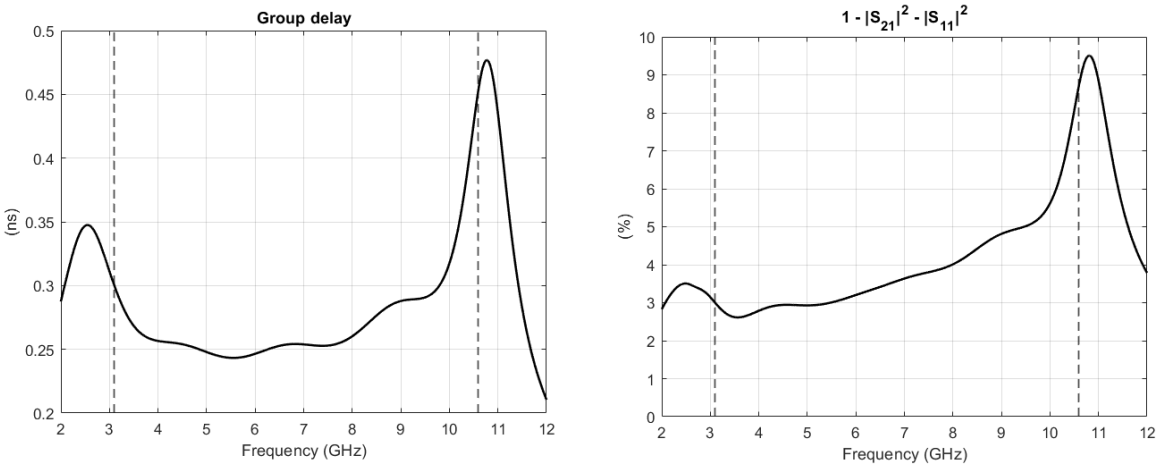

(a) (b)

Figure 4.8. Ultra-wideband filter with embedded filtering stages. (a) Group Delay and (b) Power Balance.

4.3. STEPPED IMPEDANCE RESONATOR (SIR)

It is commonly known that a half-wavelength open-circuited transmission line acts as a resonator with resonance frequencies occurring when the electrical length is

$$\theta_T = n\pi, \tag{4.1}$$

being n the number of the resonant mode [21].

These resonators, referred to as uniform impedance resonators (UIRs), exhibit constant impedance along their structure.

From Eq. (4.1), it can be deduced that the harmonic resonances of uniform impedance resonators occur at integer multiples of its fundamental resonant frequency. This limits its applicability in scenarios demanding precise control over the harmonic spectrum, such as in the design of wideband filters.

Stepped impedance resonators (SIRs) are non-uniform resonators that address this issue. Their possible configurations are depicted in Figure 4.9, alongside a comparison with the uniform impedance case.

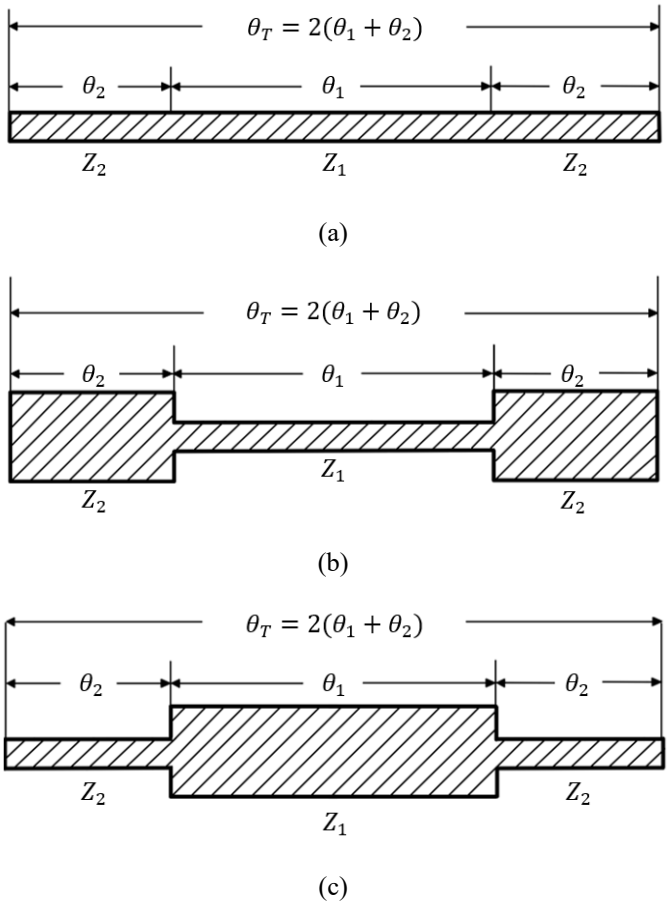

Figure 4.9. Open-circuited half-wavelength transmission line resonator configurations. (a) UIR (K=1). (b) Type I SIR (K<1). (c) Type-II SIR (K>1). Source: [21].

As observed, the SIR is a symmetric resonator composed of two line sections with different characteristic impedances, Z_1 and Z_2, and electrical lengths, θ_1 and θ_2.

The impedance ratio is defined as $K = Z_2/Z_1$, and the fundamental resonance condition is [22]:

$$K = tan\theta_1 \cdot tan\theta_2 \tag{4.2}$$

In practice, it is typically preferred to set $\theta_1 = \theta_2 = \theta$ to simplify the calculations. With this, from Eq. (4.2) it can be deduced that the electrical length $\theta(f_1)$ corresponding to the fundamental resonance frequency f_1 is given by [22]

$$\tan^2 \theta(f_1) = K \tag{4.3}$$

so that

$$\theta(f_1) = \tan^{-1}\sqrt{K} \tag{4.4}$$

Although it is not the focus of this project, an analysis of the equivalent circuit of a stepped impedance resonator reveals that the even-mode and odd-mode resonant frequencies of the SIR are [21]:

$$\begin{aligned} K - tan\theta_1 \cdot tan\theta_2 = 0 \qquad & \textit{(at odd-mode frequencies)} \\ K \cdot tan\theta_1 + tan\theta_2 = 0 \qquad & \textit{(at even-mode frequencies)} \end{aligned} \tag{4.5}$$

so the electrical lengths of the non-fundamental resonant frequencies for the case with $\theta_1 = \theta_2 = \theta$ can be obtained:

$$\theta(f_2) = \frac{\pi}{2} \tag{4.6}$$

$$\theta(f_3) = \pi - \tan^{-1}\sqrt{K} \tag{4.7}$$

$$\theta(f_4) = \pi \tag{4.8}$$

It is interesting to express the resonance frequencies normalized with respect to the fundamental frequency, as this approach enables an understanding of how the separation between them can be controlled based on the impedance ratio $K = Z_2/Z_1$:

$$\frac{f_2}{f_1} = \frac{\theta(f_2)}{\theta(f_1)} = \frac{\pi}{2\tan^{-1}\sqrt{K}} \tag{4.9}$$

$$\frac{f_3}{f_1} = \frac{\theta(f_3)}{\theta(f_1)} = \frac{\pi}{\tan^{-1}\sqrt{K}} - 1 \tag{4.10}$$

$$\frac{f_4}{f_1} = \frac{\theta(f_4)}{\theta(f_1)} = \frac{\pi}{\tan^{-1}\sqrt{K}} \tag{4.11}$$

These expressions have been represented graphically using MATLAB, resulting in Figure 4.10. This plot clearly illustrates that as the parameter *K* decreases from unity, higher-order resonances shift further away in frequency from the fundamental resonance. Conversely, increasing *K* results in these resonances shifting progressively closer to the fundamental one. Furthermore, it is significant to note that the case where $K = Z_2/Z_1 = 1$ corresponds to the uniform impedance resonator (UIR), in which the resonances occur at integer multiples of the fundamental resonance, as explained before.

The above-mentioned properties of SIRs allow manipulation of the impedance ratio *K* to design filters where the spurious band shifts away in frequency, thereby increasing the upper stopband bandwidth. Alternatively, higher-order resonances can be brought closer to the fundamental one to achieve filters

with a wider passband, as will be examined in the following sections. Specifically, this latter approach leads to the development of the so-called multiple-mode resonators, since multiple resonant frequencies are simultaneously excited.

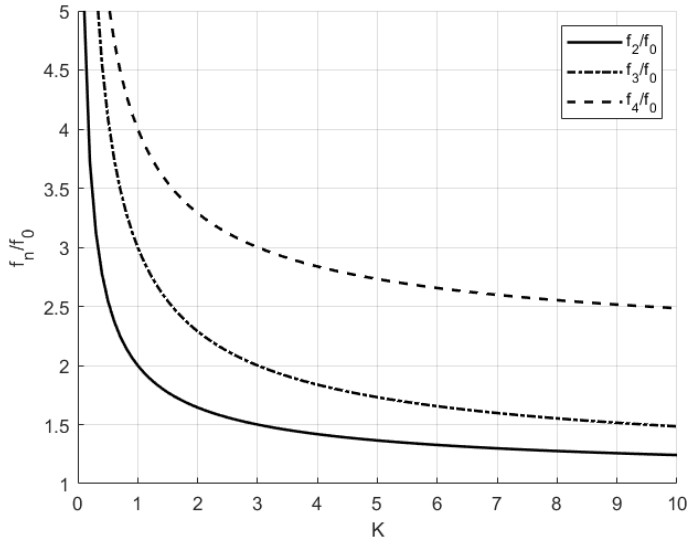

Figure 4.10. Normalized resonance frequencies of the SIR ($\theta_1 = \theta_2 = \theta$).

4.4. MULTIPLE MODE RESONATOR (MMR) FILTERS

As introduced at the end of the previous section, multiple-mode resonator filters are those in which the dimensions or topologies of the lines are manipulated to bring the resonances closer to the fundamental one. When combined with sufficiently strong input and output coupling, this approach enables the realization of an ultra-wide passband with significantly low insertion loss level [23].

In particular, it has been demonstrated that increasing the impedance ratio K of a SIR produced this effect, giving rise to multi-mode stepped impedance resonator filters. These filters are physical structures based on segments with different impedances, as presented in the previous section, which support multiple resonant modes.

It should be noted that a SIR may operate as a MMR if it is designed to support multiple useful resonant modes within the interest band, but not all the SIR are MMR, since there are cases in which it is desirable to increase the separation between spurious frequencies and the fundamental, and not all MMRs are SIRs, since various alternative methodologies exist for combining resonant modes within the passband.

This concept of filter is exploited in chapters 5 and 6, together with the characteristics of the SIRs discussed in the previous section, for the development of the two final designs of this project.

4.5. STUDY OF A COMPACT HIGH-TEMPERATURE SUPERCONDUCTING (HTS) STUB-LOADED MULTI-MODE RESONATOR (MMR) ULTRA-WIDEBAND (UWB) FILTER

This section aims to study a complex filter extracted from the literature, whose frequency response covers a large portion of the spectrum assigned to ultra-wideband communications, with considerably good performance for the challenges involved in working over such a large bandwidth. To this end, its main characteristics and components have been analyzed and understood, and several studies have been conducted in an attempt to improve its performance.

The filter under consideration was originally proposed in [24], so most of the theoretical concepts involved and the figures presented in this section are based on that article.

The layout of the structure is shown in Figure 4.11.

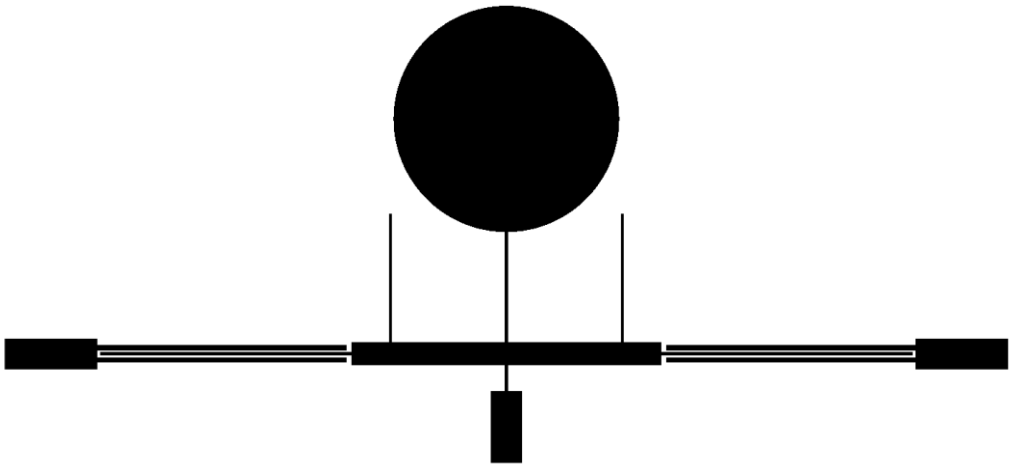

Figure 4.11. Layout of HTS stub-loaded MMR UWB filter under study. Adapted from: [24].

It can be observed that the main component of the filter is a stepped impedance resonator of type II, as the one presented in Figure 4.9. This resonator is connected to the input and output transmission lines by interdigital-coupled feed lines, which provide sufficiently strong coupling to achieve ultra-wideband behaviour, as well as two extra poles and a transmission zero in the upper stopband.

In the center of the structure, two stepped impedance resonators can be observed in the vertical axis. The lower one produces a transmission zero at a frequency close to 12 GHz, thus improving rejection in the upper stopband, and also introduces a new transmission pole in the passband. In the upper resonator, which is also of the stepped impedance type, the conventional low-impedance section has been replaced by a circular patch in order to reduce the number of design parameters, which is useful when optimizing to reduce the required time. This resonator also generates a transmission maximum within the band of interest and is responsible for introducing a zero around 2.5 GHz, thus enhancing rejection in the lower stopband.

Finally, the pair of symmetric stubs generates a new transmission zero around 14.5 GHz, which also improves the filter's selectivity.

With all these features, the designers of the original filter achieved the following result, directly extracted from the cited article. Figure 4.12 shows all the characteristics described, as well as the influence of each of the elements discussed.

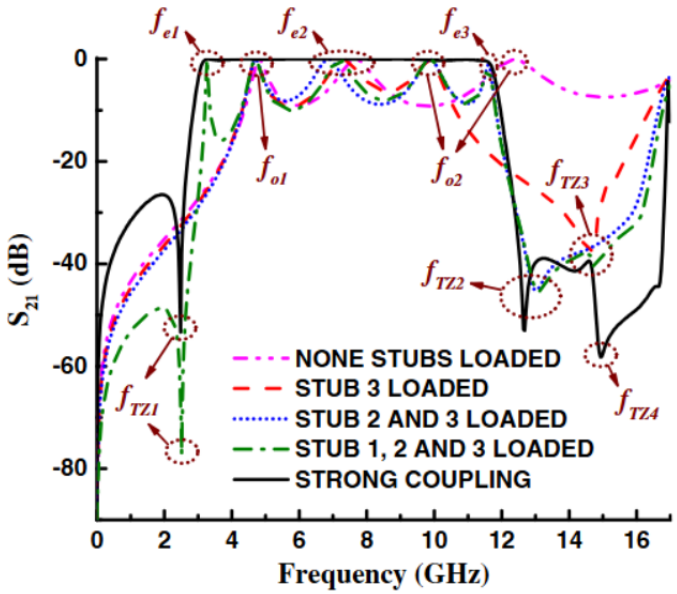

Figure 4.12. Provided response of HTS stub-loaded MMR UWB filter under study. Source: [24]

After understanding the behaviour of the filter, the next objective is to perform an electromagnetic simulation. With this, it is intended to compare the obtained result with the provided one to verify that the port definitions, radiation box, and meshing settings are appropriate, as this configuration will be used in future designs.

To this end, Ansys HFSS software has been employed. As in the previous sections, in addition to the developed automation scripts to draw the 3D structure, shown in Figure 4.13.

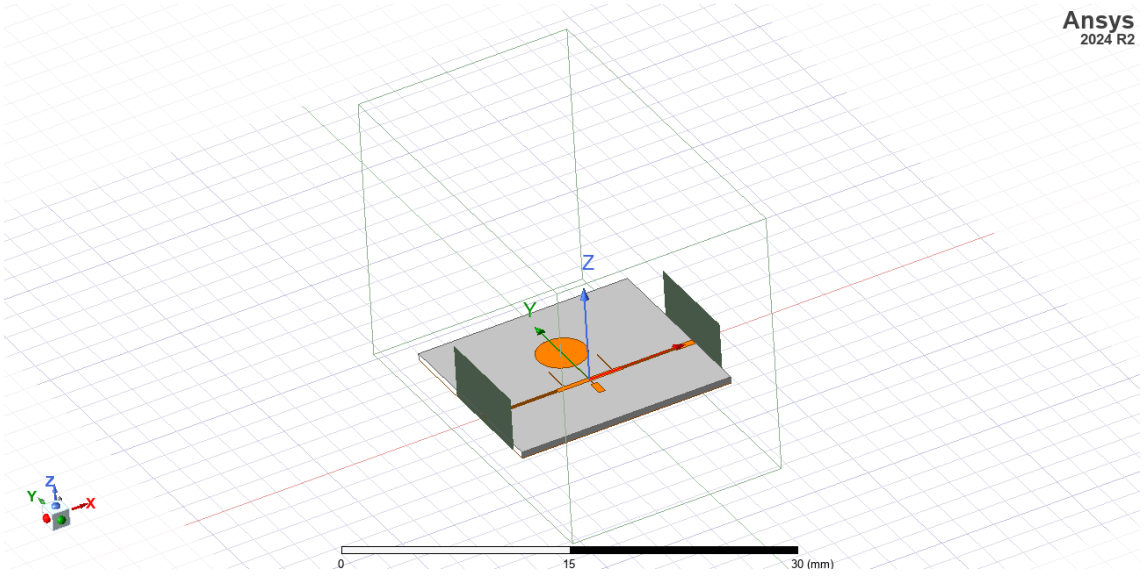

Figure 4.13. Electromagnetic model of HTS stub-loaded MMR UWB filter under study.

As it can be observed, the wave ports have been defined as shown in Figure 3.4. The simulation volume has been set with a distance of $\lambda/4$ at 17 GHz of the simulation from any radiation edge of the structure on the Y-axis, and a distance of $3\lambda/4$ on the positive Z-axis, as in Section 4.5.

This choice is based on the assumption that radiation along Y-axis will be minimal, since in microstrip technology designs the fields are mainly confined in the interface between the substrate and the conductor, being the Z-axis the critical direction. In the negative Z-axis the distance has been set to zero, as an infinite ground plane has been defined.

These considerations allow to considerably reduce the simulation volume, thus significantly accelerating time while maintaining results accuracy. This is also advantageous for the subsequent optimization process.

Due to the required precision to obtain the seven reflection zeros and the complexity of the structure, it has been necessary to define a mesh refinement with 17 passes and a frequency sweep of 3501 points.

The obtained result is depicted in Figure 4.14.

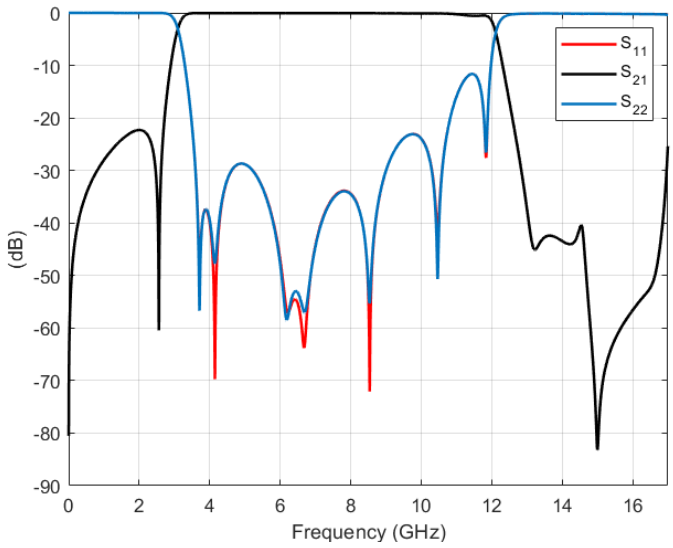

Figure 4.14. Electromagnetic simulation result of HTS stub-loaded MMR UWB filter under study.

Although the obtained response exhibits some differences compared to that reported by the authors in [24], a good approximation has been achieved, which clearly reveals the electromagnetic behaviour of the structure.

More precise results could be obtained by using a finer mesh and a discrete frequency sweep with a higher number of points. However, this would require a more powerful computer and a considerably longer simulation time. Therefore, it is considered that the simulation results are satisfactory for the established objective.

Subsequently, as mentioned before, the aim is to improve the response of the filter. The main idea is to replace the circular patch resonator with a spiral-type resonator, either rectangular or circular, as this has a greater number of design parameters, such as the feed position, the width of the spiral, the number of turns, or the distance between turns, which allows more precise control over the entire filter response.

Figure 4.15 shows the layout of the described resonators.

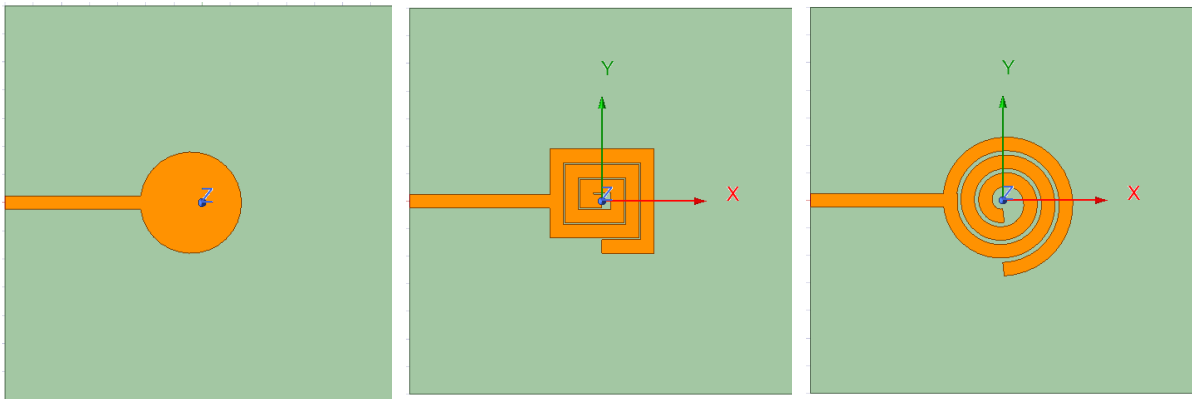

(a) (b) (c)

Figure 4.15. Layout of (a) circular patch, (b) rectangular spiral and (c) circular spiral.

By modifying the effective length of the spiral, the resonance frequency can be controlled. Additionally, the resonance bandwidth, directly related to the quality factor Q, and the depth of the minimum in dB can be adjusted through the spacing between turns, the number of turns, and the coupling. Therefore, it is first necessary to understand how each parameter affects to the behaviour of the resonator, for which a comprehensive study for each of them has been conducted.

Figure 4.16 shows the obtained results as a function of the feed position, the width of the spiral, the number of turns and the distance between turns.

It is clear to see how the separation between turns is a critical parameter that shifts the resonance frequency and also affects the coupling strength, reflected in the depth of the s_{11} minimum. This occurs because greater separation reduces the coupling capacitance between adjacent section, which increases the resonance frequency and decreases the coupling efficiency, while the opposite occurs with less separation. This parameter also affects to the total inductance due to greater mutual coupling between adjacent turns [25].

On the other hand, as the width increases, narrower, shallower and lower frequency resonance is obtained, while low widths provide wider and deeper resonances at higher frequencies. This can be explained by the fact that a wider line decreases the inductance per unit length and increases the capacitance between turns [25].

Nevertheless, these statements are based on approximating the resonance frequency using a lumped-element circuit consisting of and inductor (L) and a capacitor (C) according to

$$f_0 \approx \frac{1}{2\pi\sqrt{LC}} \tag{4.12}$$

although the electromagnetic behaviour of the structure is more complex and unpredictable, which slightly complicated the purpose of this section.

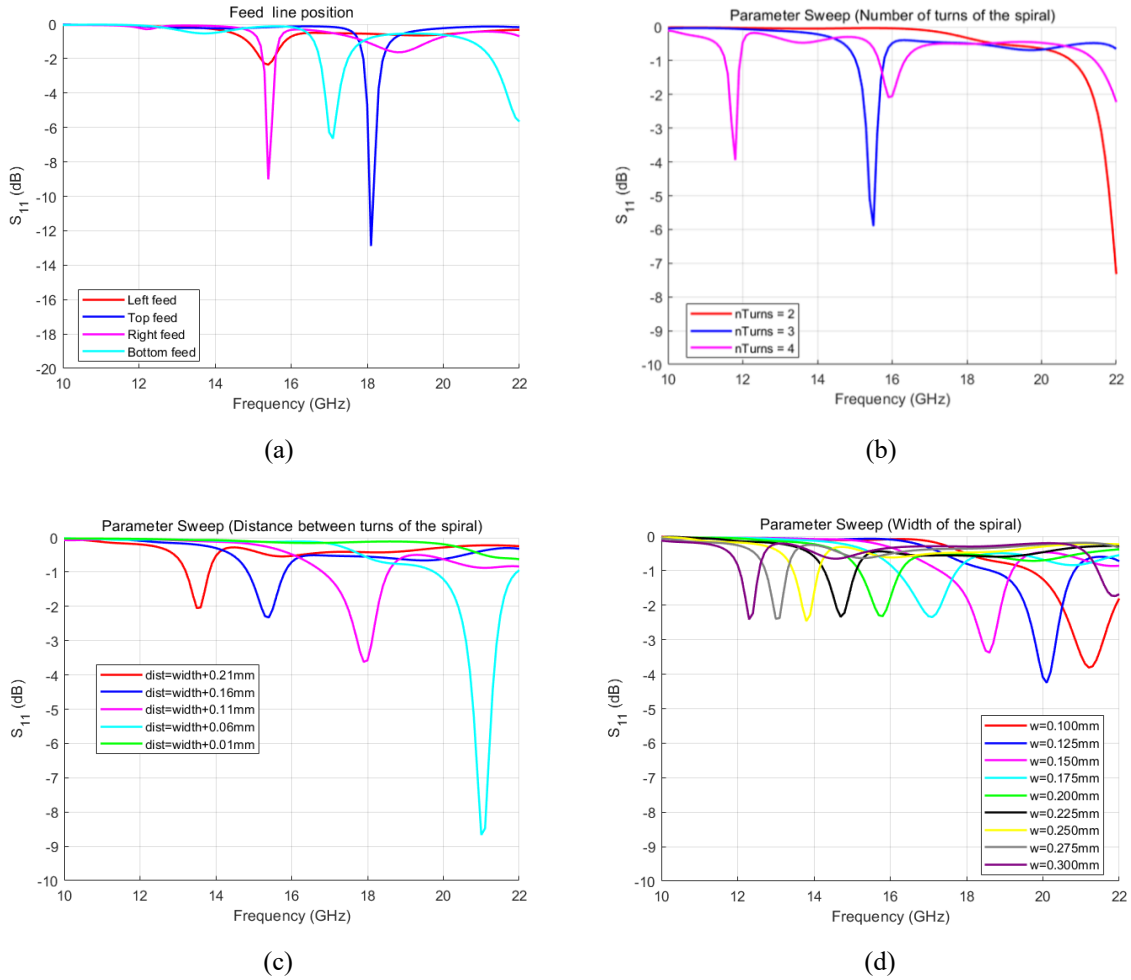

Figure 4.16. Parameter sweep of rectangular spiral parameters. (a) Feed line position, (b) number of turns, (c) distance between turns and (c) width of the spiral.

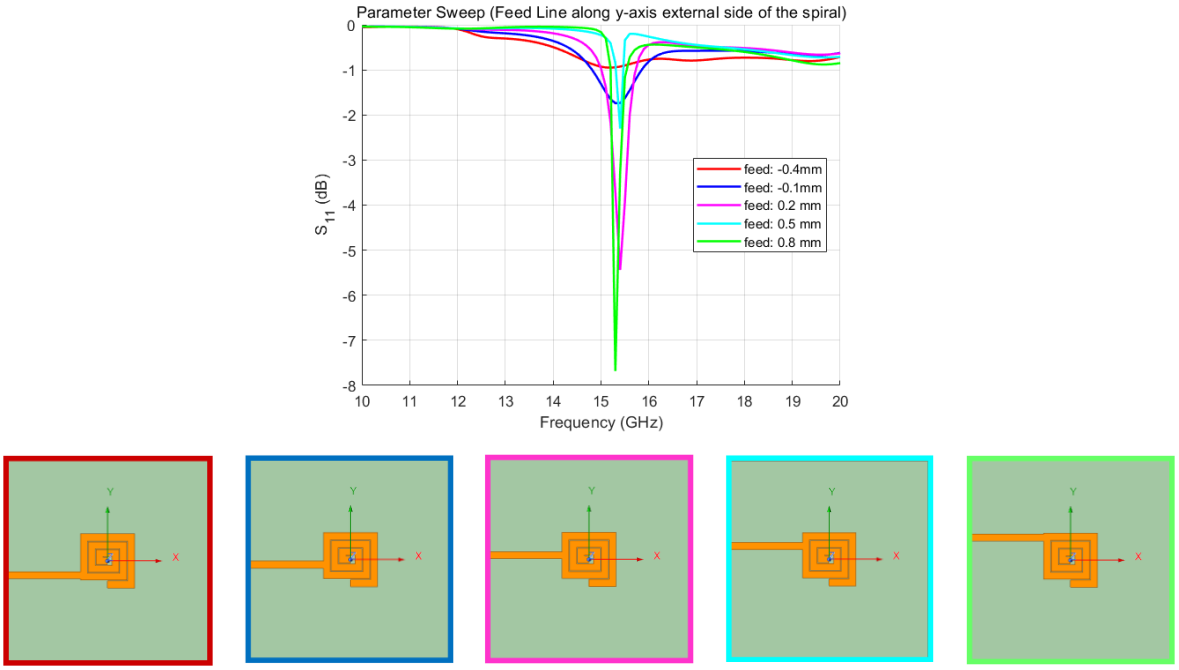

Figure 4.17. Parameter sweep of rectangular spiral: feed line position along y-axis.

Additionally, it has been verified how offsetting the feed line with respect to the spiral, that is, slightly displacing it along the same axis, as represented in Figure 4.17.

Having completed this extensive study, an approximation of the spiral resonator's response to that of the patch resonator, shown in the following figure, has been carried out, already integrated within the low-impedance section of the SIR following the layout presented at the beginning of this section.

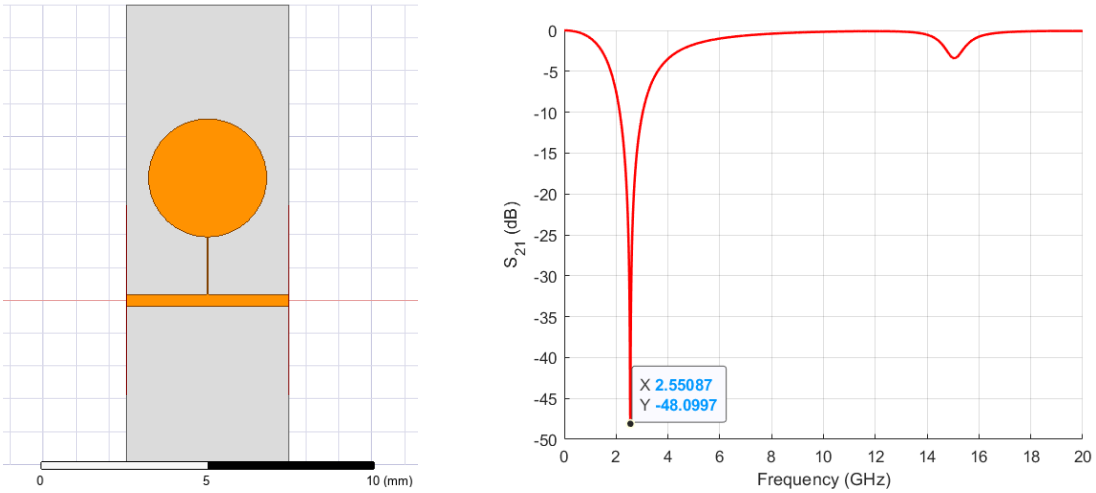

(a) (b)

Figure 4.18. Circular stepped impedance resonator. (a) Layout and (b) simulation result.

Figure 4.18 confirms the behaviour of the circular stepped impedance resonator, which introduces a transmission zero around 2.5 GHz, as already mentioned when analyzing the complete filter.

After several attempts to achieve a similar result to the previous one with a rectangular spiral, modifying the corresponding parameters based on the previous study, it has not been possible to obtain a resonance at this frequency without introducing a spurious response in the passband.

The same procedure has been also attempted with a circular spiral, but despite multiple variations, it has not been possible to separate the second resonance sufficiently to prevent it from occurring within the band of interest.

Therefore, this section concludes without having been able to improve, or even approximate, the filter response by replacing the patch with a spiral. Although many other options could be explored for this purpose, the process undertaken and the acquired knowledge are considered sufficiently valuable, and therefore is not deemed necessary to explore new alternatives within the scope of this project.

CHAPTER FIVE

Design and Implementation of a Triple-Mode Stepped Impedance Resonator (SIR) Ultra-Wideband (UWB) Filter

This chapter covers the analysis, design, and implementation of an ultra-wideband filter using the concepts discussed in Section 4.3 and the automation tools described in Section 3.2.

The design process is comprehensive, starting from the analysis stage and ending with the manufacture and measurement of the filter in a Vector Network Analyzer (VNA). To achieve this, it has been necessary to comply with the constraints imposed by the available fabrication technology, which has limited the design, as will be discussed later.

One of the main limitations is the selection of manufacturing material. Since high-temperature superconducting technology requires very complex processes and tools, this filter will be manufactured with conventional materials, which have poorer performance, as a proof of concept.

Another fabrication constraint is the minimum achievable size of the lines. Since a micro-milling machine will be used, this parameter has been set to $0.25\,mm$, in accordance with the in-house manufacturing capabilities, which significantly restricts the design process.

Nevertheless, those limitations allow for a comparison between the results obtained with this material and those that could be achieved using HTS technology. This is of great interest since it highlights the advantages of superconducting technology, which is the main objective of the project.

5.1. FILTER DESIGN

A fifth-order ultra-wideband filter based on a stepped impedance resonator in microstrip technology is proposed. The objective of this design is to achieve the maximum possible bandwidth within the band of interest ($3.1\,GHz - 10.6\,GHz$), given the aforementioned limitations.

In this design, the dielectric material Rogers RO4350B will be used, with a thickness of $0.76mm$ and a conductor with a thickness of $35\mu m$. The provided relative permittivity of the substrate by the manufacturer is 3.48 ± 0.05, and the loss tangent at $10\,GHz$ is 0.0037, as depicted in Figure 5.1.

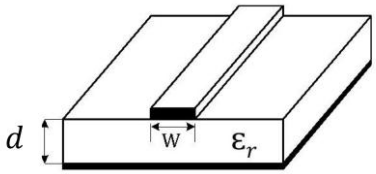

$d = 0.76\,mm$

$\varepsilon_r = 3.48$

$tan\delta = 3.7 \cdot 10^{-3}$

Figure 5.1. Microstrip line technology for the fabrication of the SIR UWB filter. Source: [26].

As seen in Section 4.3, stepped impedance resonator filters are based on manipulating the impedance ratio K of the resonator. To this end, it is necessary to establish the range of impedances that can be achieved given the technology used.

For a microstrip line, there is a relationship between the characteristic impedance of the line and its width, which is given by the following expression [10]:

$$Z_0 = \begin{cases} \frac{60}{\sqrt{\varepsilon_{r_{eff}}}} ln\left(\frac{8d}{W} + \frac{W}{4d}\right) & para\ \frac{W}{d} \leq 1 \\ \frac{120\pi}{\sqrt{\varepsilon_{r_{eff}}}\left[\frac{W}{d} + 1.393 + 0.667\ ln\left(\frac{W}{d} + 1.444\right)\right]} & para\ \frac{W}{d} \geq 1 \end{cases} \quad (5.1)$$

being $\varepsilon_{r_{eff}} = \frac{\varepsilon_r+1}{2} + \frac{\varepsilon_r-1}{2}\frac{1}{\sqrt{1+\frac{12d}{W}}}$ the effective permittivity of the line.

Plotting this relationship in MATLAB, Figure 5.2 is obtained, in which it is deduced that the useful impedance range is between 20Ω and 120Ω, as higher impedance levels require very high manufacturing precision, while lower impedances would result in excessively wide lines.

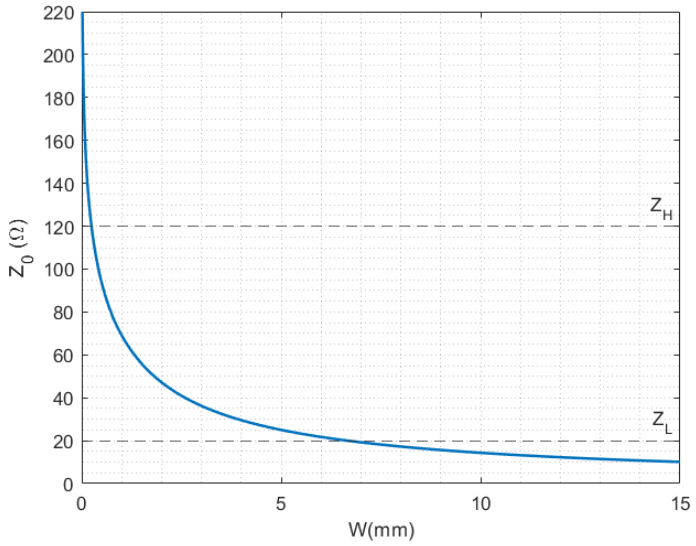

Figure 5.2. Relationship between width and characteristic impedance of a microstrip line.

The next step is to obtain the impedance ratio. In Figure 4.10 it can be observed that for $K = Z_2/Z_1 = 0.741398$ and fixing the fundamental resonance at $f_1 = 3.1\ GHz$, the following resonances are obtained at $f_2 = f_1 \cdot 2.21 = 6.85\ GHz$ and $f_3 = f_1 \cdot 3.42 = 10.6\ GHz$, thus covering the desired band. This is represented in the following graph. In this case, given that the fundamental resonance and the next two are used to construct the passband, a triple-mode resonator is being designed. It is desirable for the fourth resonance to be as far as possible from the passband in order to improve filter selectivity. Nevertheless, this condition is not satisfied in the present design, as will be demonstrated subsequently.

This configuration has been represented with ideal transmission lines using the ADS software, based on the expressions in Section 4.3, adding a weak capacitive coupling at each port to represent an open-

ended transmission line. The obtained circuit response is depicted in Figure 5.3, where the resonance can be clearly identified and are consistent with the theoretical calculations discussed previously.

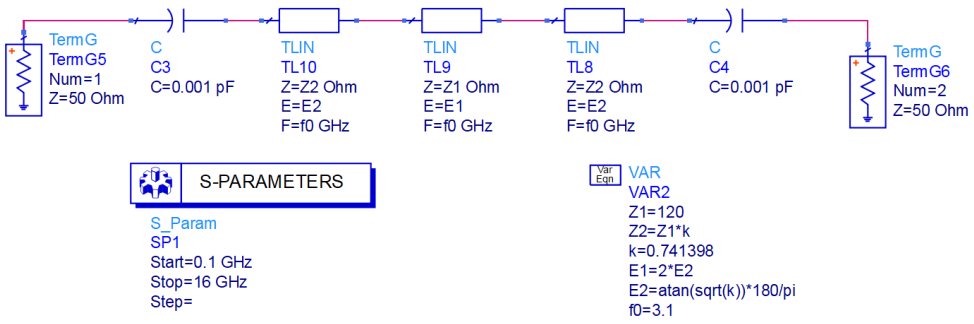

(a)

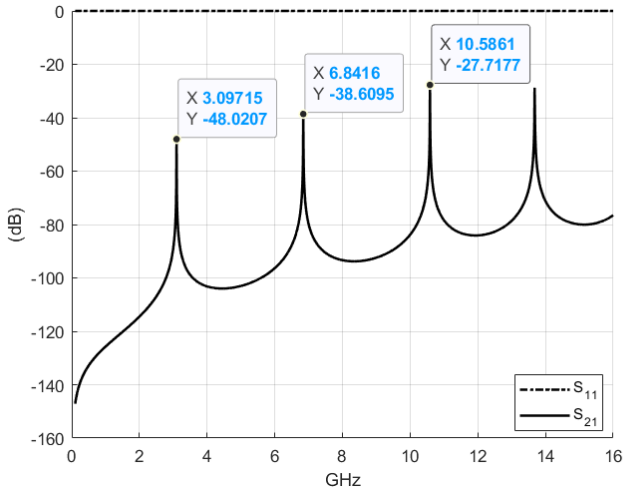

(b)

Figure 5.3. (a) Schematic and (b) circuit response of initial SIR UWB filter with ideal lines.

The next step is the realization of the prototype with real transmission lines and, after verifying that the behaviour matches the desired one, the capacitive gaps are replaced by parallel-coupled lines, obtaining a structure formed by an open-ended SIR fed by coupled sections at the input and output ports.

The schematic and layout are shown in Figure 5.4.

The filter bandwidth Δf is directly related to the loaded quality factor (Q_L), introduced in Section 2.1.4, by the expression

$$Q_L = \frac{f_0}{\Delta f} \tag{5.2}$$

being f_0 the center frequency.

Based on the previous definitions of quality factors, it can be deduced that weak input and output coupling provides a high Q_L, while strong coupling reduces Q_L. Therefore, for the design of a filter with

a wide bandwidth, a very strong coupling is required, which implies a very small gap between the coupled lines.

In this case, since the minimum dimension is restricted to be $0.25\,mm$, as explained before, the achieved coupling is not strong enough, making it not possible to obtain a bandpass behaviour with the resonance frequencies fixed previously.

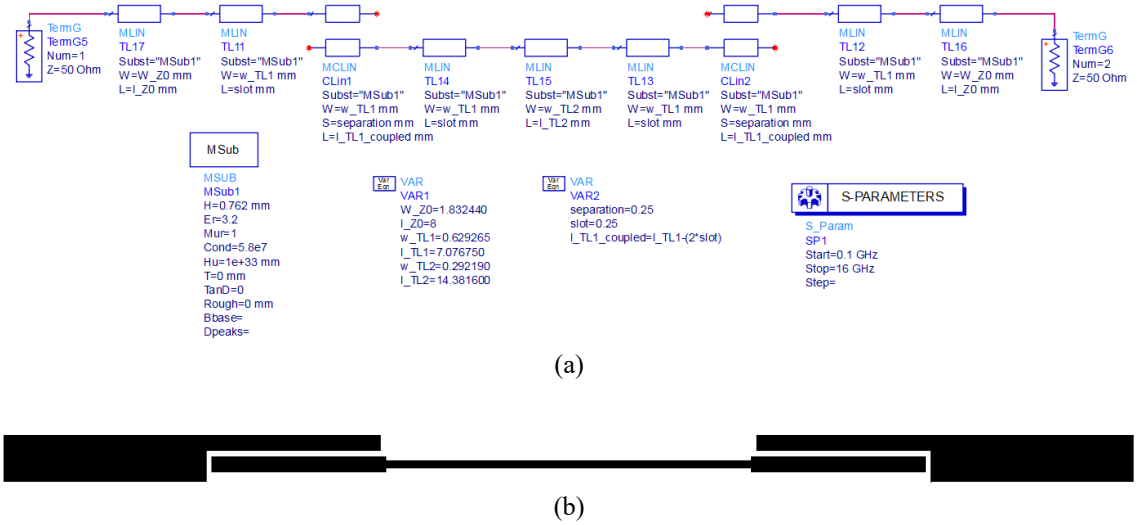

(a)

(b)

Figure 5.4. (a) Schematic and (b) layout of initial SIR UWB filter with real lines and parallel I/O coupling.

Figure 5.5 illustrates the filter response as a function of the separation between the parallel-coupled lines, denoted by G_c. It is evident that the response improves as this parameter decreases, ultimately requiring an unfeasible separation. Moreover, simulations have shown that with a sufficiently strong coupling, two extra poles can be achieved, as will be demonstrated in later results.

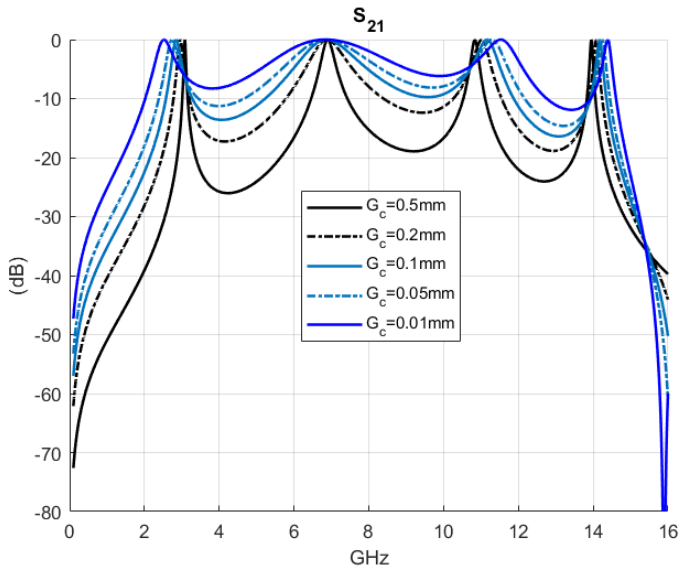

Figure 5.5. Circuit response of initial SIR UWB filter with real lines as a function of separation of parallel I/O coupling sections.

Therefore, given the limitations of the available technology, it is necessary to bring closer the spurious resonances to the fundamental one in order to decrease the desired filter bandwidth and, at the same time, reduce the requirements for input and output coupling.

The proposed solution is to change the type of SIR from type I to type II, with $K > 0$, for obtaining the behaviour explained above.

In Figure 4.10 it can be observed that for $K = Z_2/Z_1 = 3.3$ and fixing the fundamental frequency to $f_1 = 3.1\,GHz$, the second and third resonances occur at $f_2 = f_1 \cdot 1.47 = 4.56\,GHz$ and $f_3 = f_1 \cdot 1.94 = 6.02\,GHz$.

Following the same procedure as in the initial case, the ideal transmission lines and real transmission lines prototypes are obtained, whose schematics and responses are shown below in Figure 5.6.

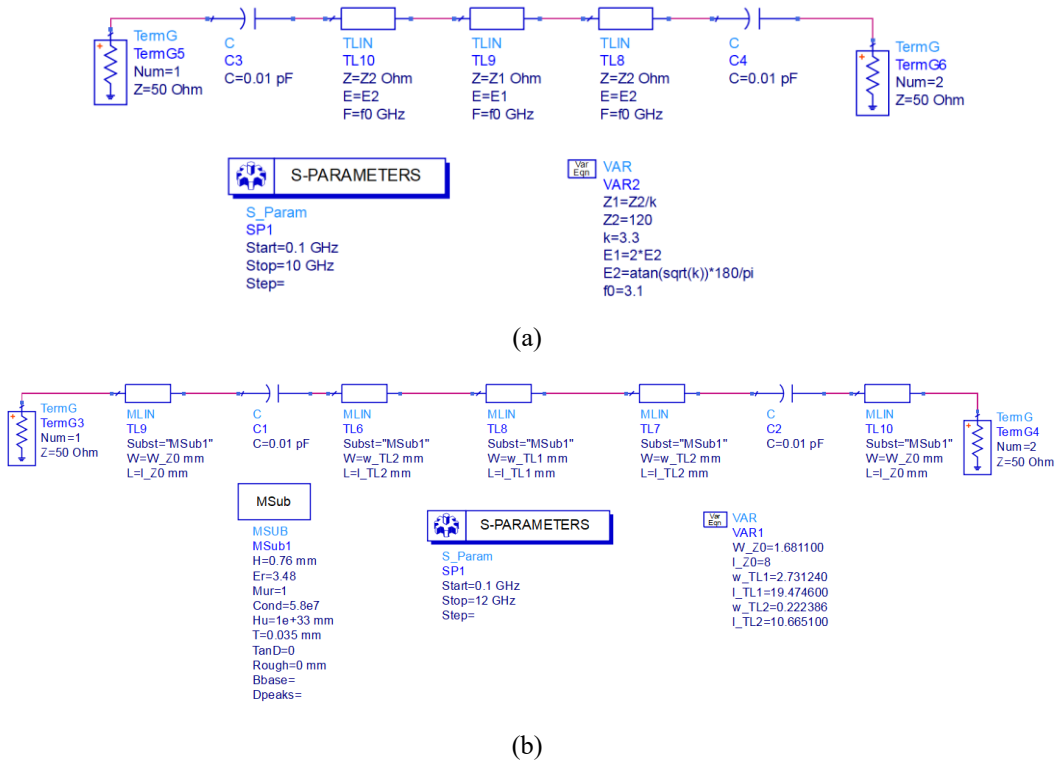

Figure 5.6. Schematic of type-II SIR UWB filter with (a) ideal lines and (b) real lines.

By comparing Figure 5.7 with Figure 5.3, it can be observed that the second and third resonances of the SIR have been brought closer to the fundamental frequency, while the fourth resonance has been shifted away from the passband.

From Eqs. (4.9) and (4.11) it is deduced that the fourth resonance occurs at twice the frequency of the second resonance. This will be reflected in the appearance of a spurious response near the passband.

Once it has been verified that the response meets the desired specifications, the design of the prototype with parallel-coupled lines at the input and output ports is carried out, as done before.

Figure 5.8 shows the circuit optimization of design variables with ADS software.

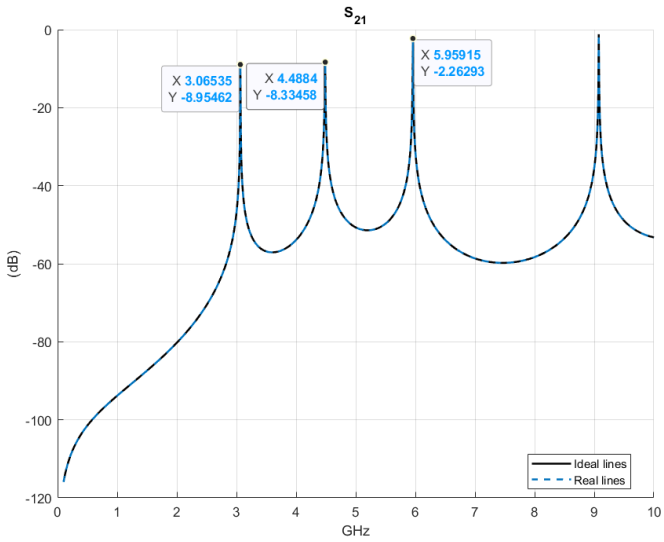

Figure 5.7. Circuit response of type-II SIR UWB filter. Ideal lines vs. real lines.

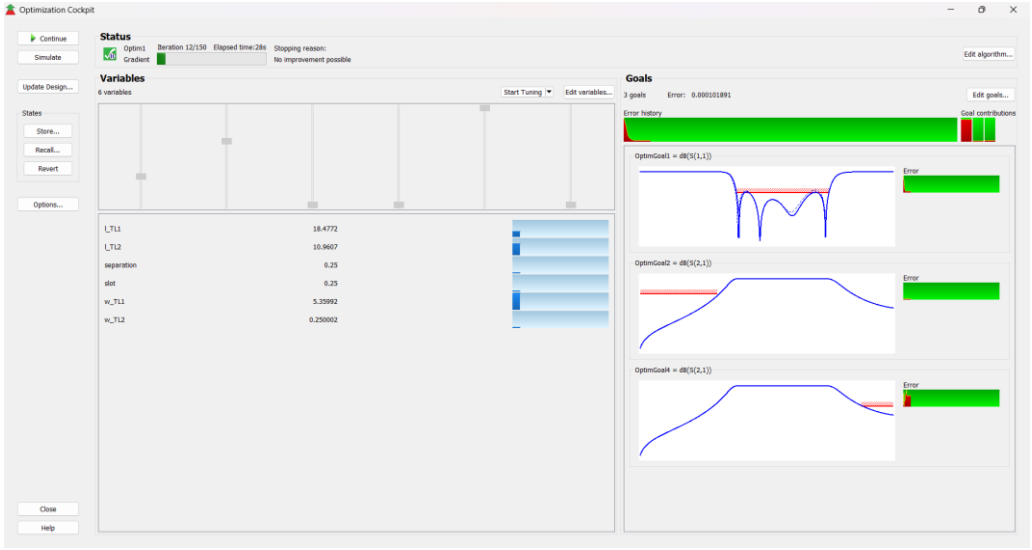

Figure 5.8. Circuit optimization of type-II SIR UWB filter with parallel I/O coupling using ADS software.

After optimization, the resulting schematic and behaviour is as depicted in Figures 5.9 and 5.10.

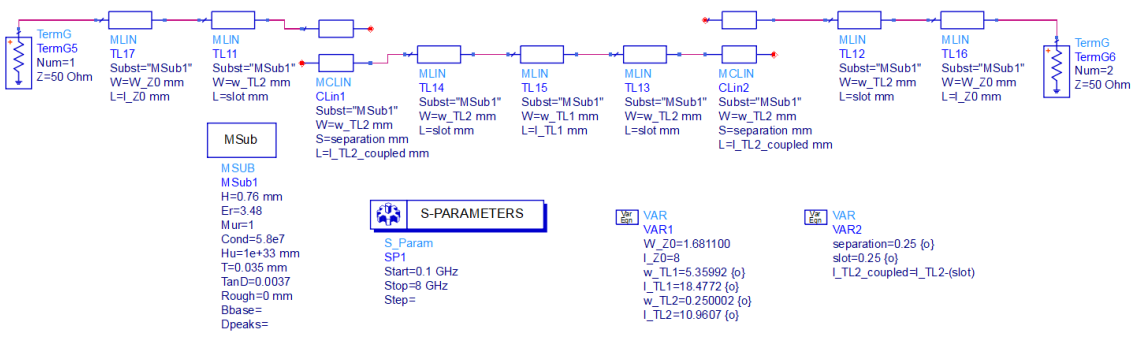

Figure 5.9. Schematic of type-II SIR UWB filter with parallel I/O coupling using ADS software.

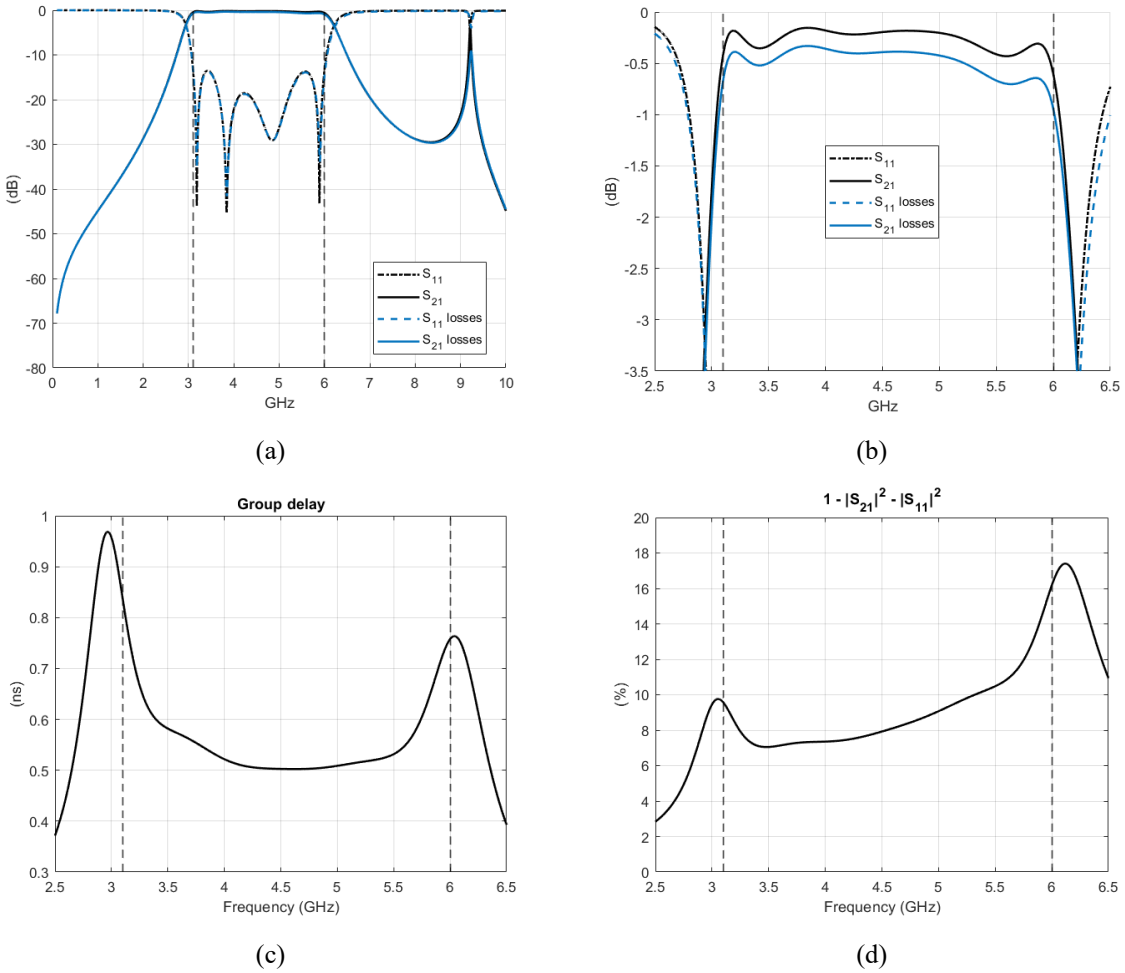

Figure 5.10. Circuit simulation results of type-II SIR UWB filter with parallel I/O coupling. (a) S- parameters: lossless vs. lossy lines. (b) Insertion loss level. (c) Group delay. (d) Power balance.

As it can be observed in the previous figure, an ultra-wideband response has been achieved, with a passband between 3.1 GHz and 6 GHz. In this frequency range, return loss level is better than 13.5 dB, and insertion losses maintain below 1 dB.

On the other hand, the group delay variation within the band of interest is less than 0.4 ns, and the losses reach up to 17% of the total power. This is primarily due to the material used. As mentioned, the use of conventional materials implies larger structures with higher losses than those achievable with HTS technology.

By comparing the dimensions of the layout in Figure 5.11 with those in Figure 4.5, although different filters are being considered, the difference in structure size as a function of the technology employed can be clearly noted.

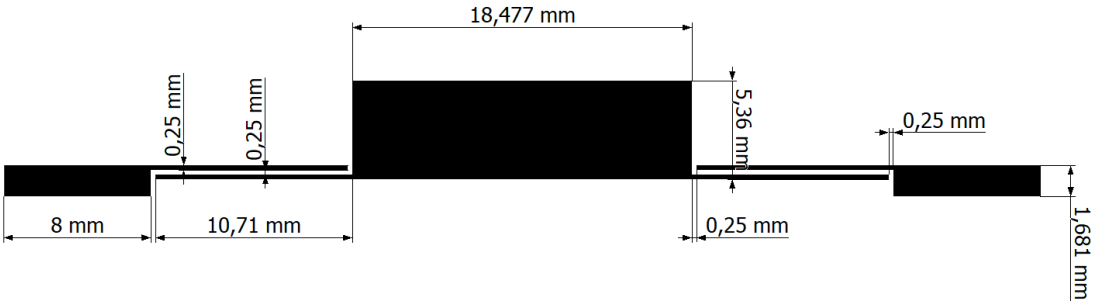

Figure 5.11. Layout of type-II SIR UWB filter with parallel I/O coupling.

5.2. ELECTROMAGNETIC MODELLING AND SIMULATION OF THE FILTER

The next step is the electromagnetic simulation of the filter, for which Ansys HFSS software has been used.

Figure 5.12 presents the 3D model with the radiation box and ports.

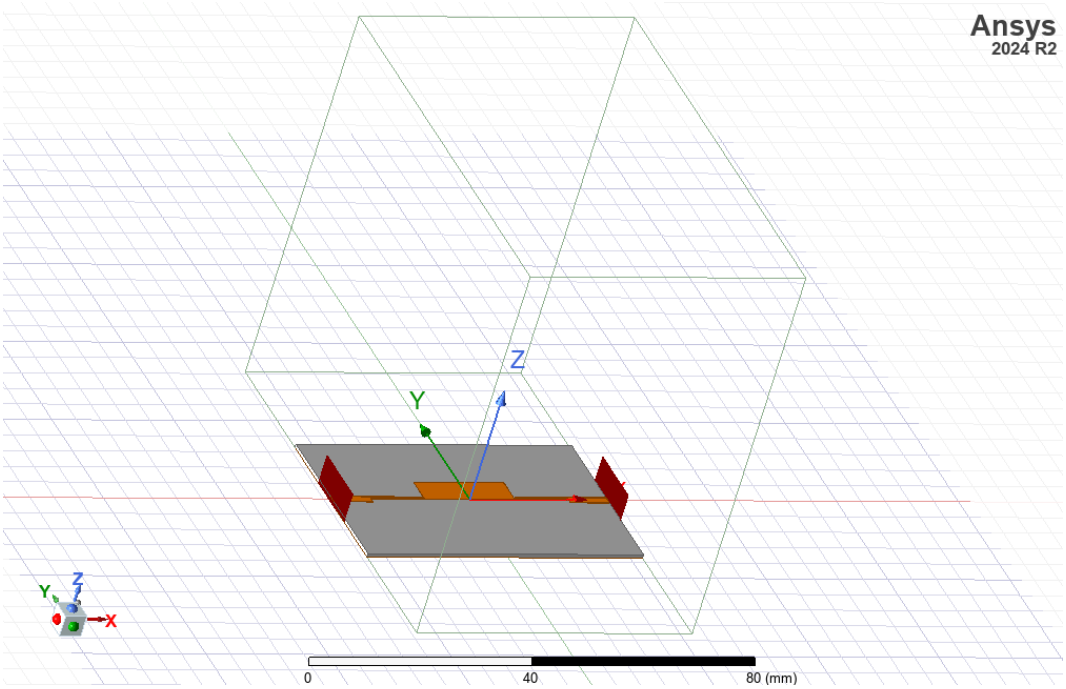

Figure 5.12. Electromagnetic model of type-II SIR UWB filter with parallel I/O coupling.

The wave ports have been defined according to the configuration shown in Figure 3.4, and the radiation box has been set with a distance of $\lambda/4$ at the maximum frequency of the simulation from any radiation edge of the structure on the Y-axis, and a distance of $3\lambda/4$ on the positive Z-axis, as in Section 4.5, based on the verification of result convergence with this configuration.

In addition, an automatic mesh refinement with 15 passes has been established, and after verifying results convergence, the filter response has been exported.

Figure 5.13 shows the comparison between the electromagnetic response and the circuit response of the structure. They clearly show that the bandwidth of the filter has been reduced, and its response has been slightly shifted downward in frequency. Furthermore, return loss level has decreased by approximately $3\,dB$, and insertion losses by about $0.3\,dB$. This behaviour was expected, since electromagnetic simulation accounts for coupling effects, discontinuities, and radiation, among other phenomena, which is not considered in the circuit model.

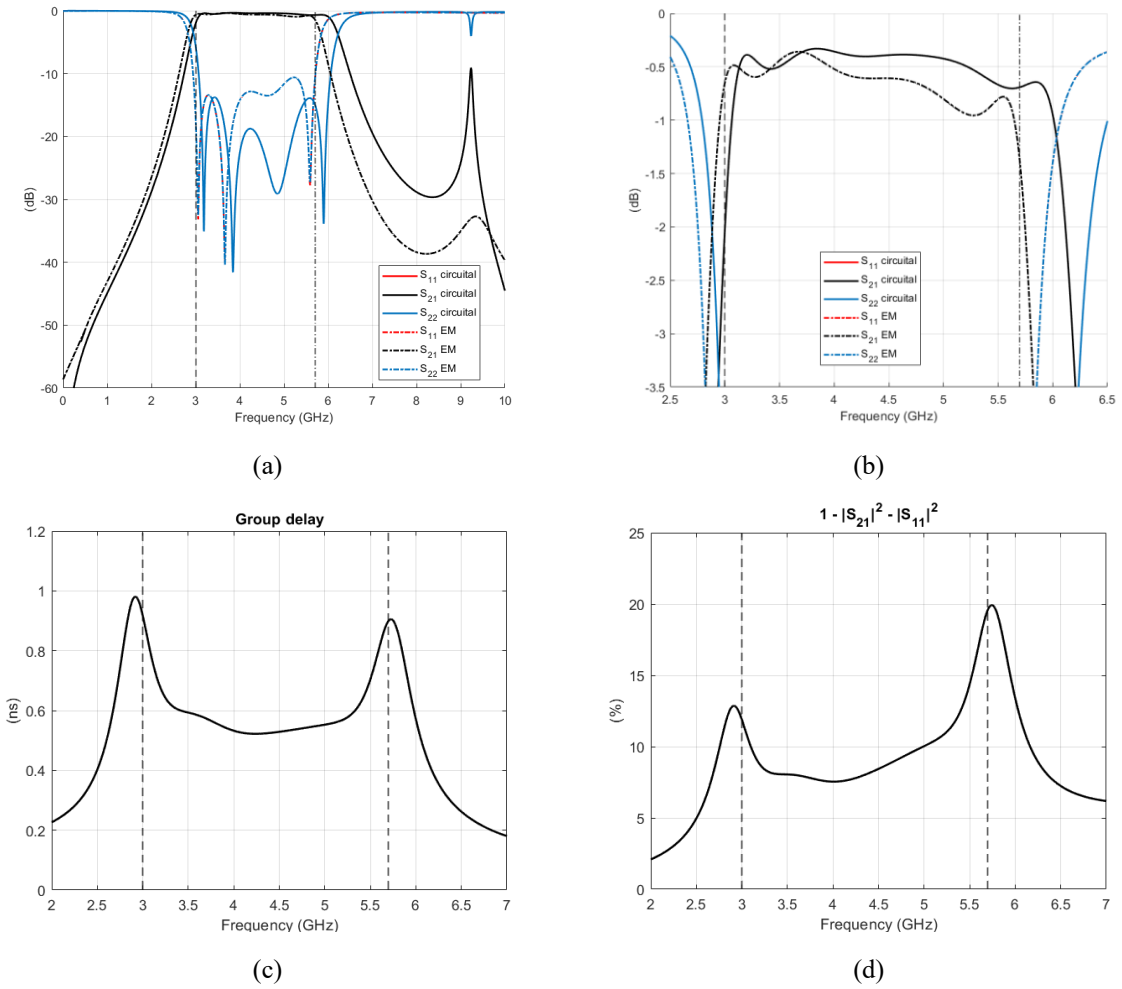

Figure 5.13. Electromagnetic simulation results of type-II SIR UWB filter with parallel I/O coupling. (a) S- parameters: circuit vs. EM. (b) Insertion loss level: circuit vs. EM. (c) Group delay. (d) Power balance.

With regard to group delay, the variation within the band of interest is similar to that of the circuit response, and the total losses increase up to 20%.

After analyzing these results, an electromagnetic optimization has been performed in Ansys HFSS using the automation tools described in previous chapters. However, as shown in the following figures, it has not been possible to increase the filter bandwidth without also increasing insertion loss, nor to improve the return loss level or the out-of-band rejection without exceeding the fabrication limits, as can be observed in Figure 5.14. Therefore, since the previous result satisfies the main objectives of the project, the design stage is concluded.

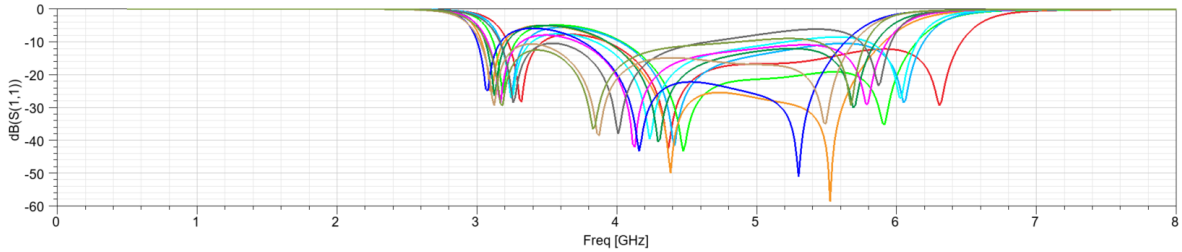

(a)

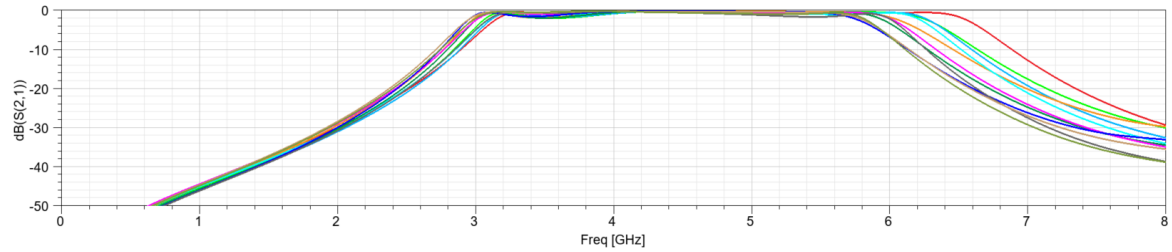

(b)

Figure 5.14. Electromagnetic optimization results of type-II SIR UWB filter with parallel I/O coupling. (a) S11. (b) S21.

5.3. FILTER FABRICATION

Once the electromagnetic response of the filter has been obtained and it has been verified that it is similar to the circuit one, the filter has been fabricated using a micro-milling machine from LPKF Laser & Electronics. The process consists of engraving the outline of the filter on the top copper layer of a Rogers RO4350B substrate, followed by the removal of the excess copper surrounding the contour. The fabrication result is shown below, including the soldered coaxial SubMiniature version A (SMA) connectors of 50Ω for the subsequent measurement process.

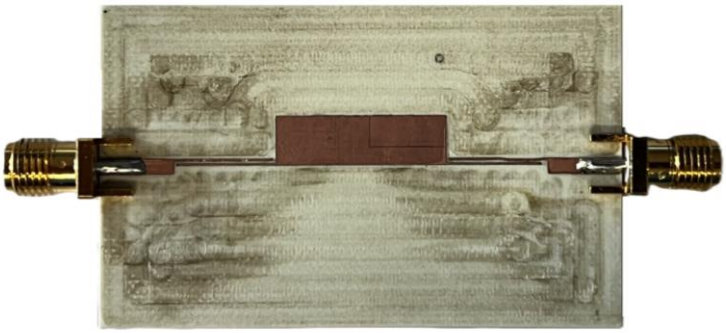

Figure 5.15. Fabricated type-II SIR UWB filter with parallel I/O coupling.

Upon close inspection of Figures 5.15 and 5.16, it can be noted a fabrication error in the parallel-coupled lines of the output port, as they are not straight and the spacing is non-uniform. This can significantly affect the filter measurement, since this separation is one of the most critical design parameters, as discussed previously.

(a) (b)

Figure 5.16. Fabrication error. (a) Input vs. Output parallel-coupled lines.

Nevertheless, it has been confirmed that the lines do not touch after a microscopic inspection, which would otherwise severely degrade the filter response.

5.4. FILTER MEASUREMENT

The last step of this chapter is the filter measurement. For this purpose, the device has been connected to the vector network analyzer (VNA) using coaxial cables at the input and the output ports, and the system has been calibrated up to 20 GHz.

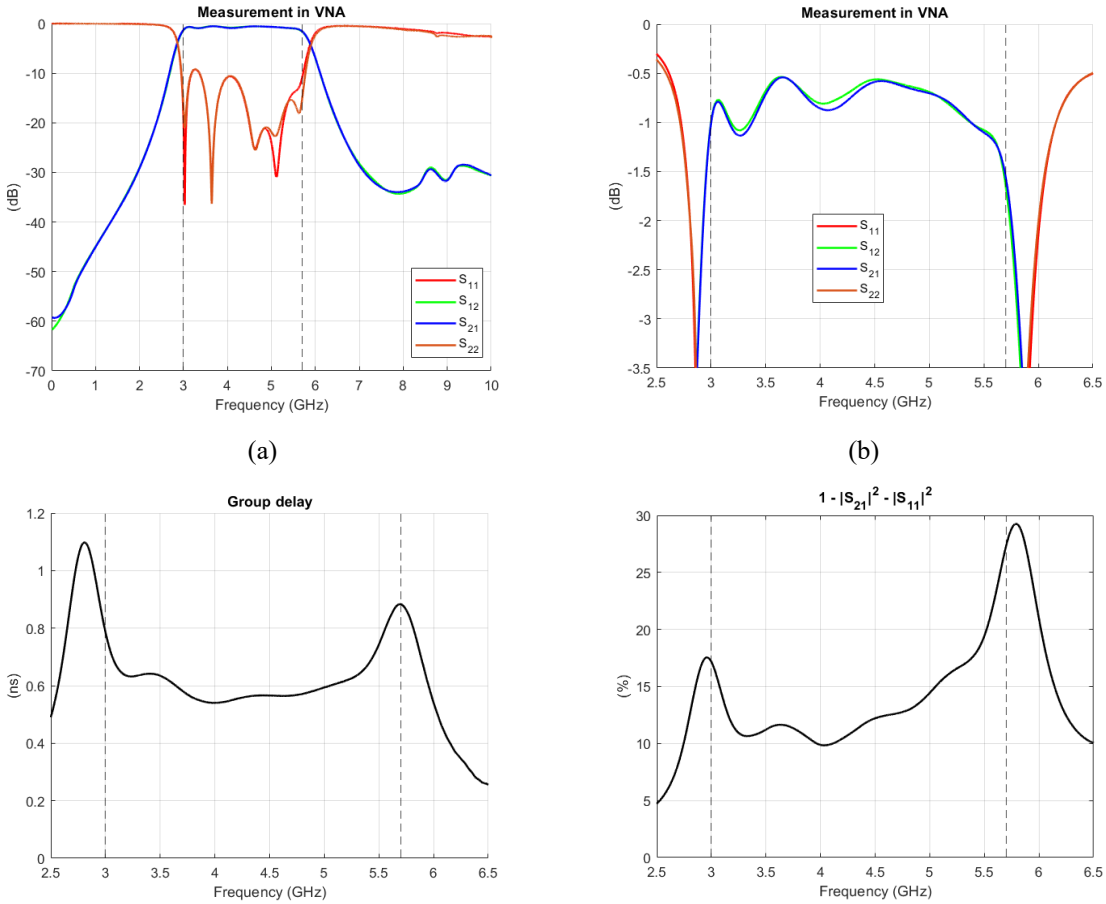

(a) (b)

(c) (d)

Figure 5.17. Measurement results of type-II SIR UWB filter with parallel I/O coupling. (a) S- parameters. (b) Insertion loss level. (c) Group delay. (d) Power balance.

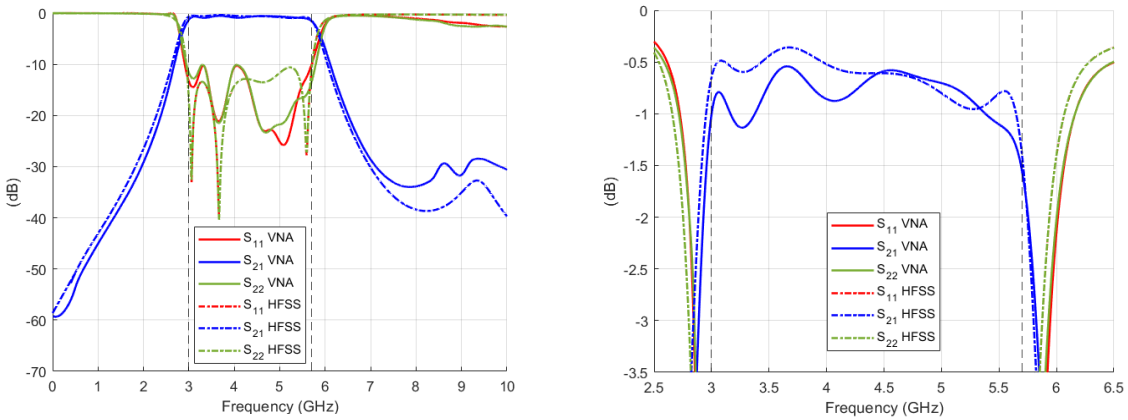

Figure 5.18. Comparison between measurement results and EM simulation results of type-II SIR UWB filter with parallel I/O coupling. (a) S- parameters. (b) Insertion loss level.

Figure 5.17 shows measurement results, to which it has been applied the *smooth* command in MATLAB in order to mitigate the ripples caused by the connectors that were not fully removed during the calibration process.

Figure 5.18 presents the comparison with the electromagnetic simulation. Both responses are highly similar, with only minor differences in the insertion loss and the return loss level.

It is noteworthy that the measurement exhibits five poles within the passband, three of which correspond to the first three resonant modes of the SIR, while the remaining two result from the coupled I/O sections, as discussed in the first section of this chapter.

In addition, the far rejection of the filter has been measured, as depicted below in Figure 5.19.

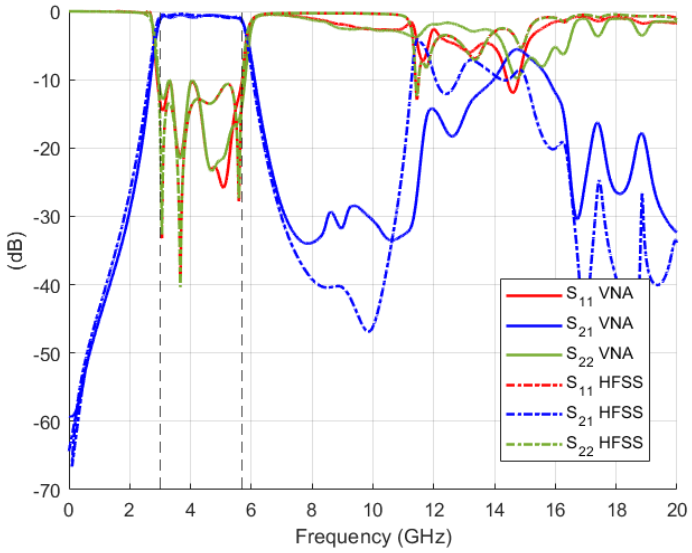

Figure 5.19. Far rejection of type-II SIR UWB filter with parallel I/O coupling. Measurement results vs. EM simulation.

As shown in the previous figure, the filter presents more than $25\ dB$ of attenuation in the upper stopband, having the first spurious at $f_{spurious} \approx 11.5\ GHz = 2.65 \cdot f_0$.

5.5. CONCLUSIONS

In this chapter, a type-II SIR ultra-wideband filter with parallel I/O coupling has been designed, fabricated and measured. The filter's performance and size have been significantly limited by the use of a conventional material. By employing high-temperature superconducting technology, a better result could have been achieved, with lower losses and a more compact structure.

Manufacturing technology also posed a major challenge in the design process, as it has been necessary to establish minimum dimensions that prevented the desired input and output couplings from being obtained. Using alternative fabrication technologies, such as laser-based processes, it would have been possible to reduce the line widths and spacing, thus achieving a response with improved selectivity, larger bandwidth, and lower insertion loss.

Nevertheless, the obtained result can be considered satisfactory given the aforementioned limitations. A filter with a passband from $3\ GHz$ to $5.7\ GHz$ has been achieved, with insertion losses below $1.5\ dB$ and a return loss level better than $9\ dB$. The group delay variation within this band is less than $0.4\ ns$, and the total losses do not exceed 30% of the total power.

Final results are summarized in Table 5.1.

BW	f_0	$BW_{\%}$	IL_{max}	RL_{min}	$Delay\ variation$	$Total\ losses$
$3.1GHz - 5.7GHz$	$4.35\ GHz$	62.07%	$1.5\ dB$	$9\ dB$	$< 0.4\ ns$	$< 30\%$

Table 5.1: Final results of type-II SIR UWB filter with parallel I/O coupling.

Moreover, the electromagnetic simulation results are very similar to the measurements obtained with the vector network analyzer, indicating a good balance between time consumption and results accuracy. In addition, it has been confirmed the correct operation of the automation tools developed.

Therefore, it can be concluded that the main objectives of this project have been successfully fulfilled during this chapter.

CHAPTER SIX

Design and Implementation of an Eight-Pole Chebyshev Ultra-Wideband (UWB) Filter with Two Triple-Mode Stepped-Impedance Resonators (SIRs)

Up to this point, it has been addressed the impact of ultra-wideband communications and the necessity of making radiofrequency filters with a broad frequency range and high selectivity, together with the emergence of high-temperature superconducting materials and their relevance in this field. The fundamentals on filter design have been studied, and various approaches for the implementation of UWB, such as cascaded filtering stages, composite structures, and stepped impedance resonators, have been explored. In addition, analysis tools and automation techniques have been developed to optimize the structures and achieve high accuracy.

This chapter aims to integrate all the concepts and tools presented throughout the project through the analysis, design and implementation of another ultra-wideband filter.

The design process is different from that described in the previous chapter, and it is intended to improve the results obtained previously, since it involves a more complex methodology. While in the previous design the impedance ratio of the resonator has been modified to directly control the resonant frequencies of the resonator, in this case two parallel SIRs are employed, whose parameters are obtained using Chebyshev synthesis.

Once again, given that the same fabrication technology is employed and HTS material are not available, the same limitations experienced in the previous design will arise, leading to a greater design challenge.

6.1. INTRODUCTION. PARALLEL COUPLED-LINE FILTERS WITH STEPPED IMPEDANCE RESONATORS

The content of this section is largely based on Chapter 12.2.4 of the book *Microstrip Filters for RF/Microwave Applications*, (Hong, 2001) [7].

The following describes the design process of parallel-coupled line filters with stepped impedance resonators, using the Chebyshev approximation. This approach leads to an equal-ripple response, whose transfer function is of the form

$$|H(j\Omega)|^2 = \frac{1}{1 + \varepsilon^2 T_n^2(\Omega)} \tag{6.1}$$

where ε is the ripple level, given by

$$\varepsilon = \sqrt{10^{\frac{L_{ar}(dB)}{10}} - 1} \tag{6.2}$$

L_{ar} is the passband ripple, while $T_n(\Omega)$ is a term that corresponds to the Chebyshev polynomials [8] [9] [26].

Although not covered in this project, it can be shown that the normalized frequencies of the poles in the passband for a Chebyshev filter are given by [7]:

$$\Omega_k = \cos\left[\frac{(2k-1)\pi}{2n}\right] \quad for\ \ k = 1,2,\dots,n \tag{6.3}$$

This expression will be employed later.

Beginning with the design process, the first step is to determine the values of the LC elements of the normalized low-pass Chebyshev prototype. These values can be obtained recursively using the following expressions:

$$g_0 = 1.0 \qquad g_i = \frac{1}{g_{i-1}} \cdot \frac{4\,sin\left[\frac{(2i-1)\pi}{2n}\right] \cdot sin\left[\frac{(2i-3)\pi}{2n}\right]}{\gamma^2 + sin^2\left[\frac{(i-1)\pi}{n}\right]} \qquad i = 2,3,\dots,n$$

$$g_1 = \frac{2}{\gamma} sin\left(\frac{\pi}{2n}\right) \qquad g_{n+1} = \begin{cases} 1.0 & n\ odd \\ coth^2\left(\frac{\beta}{2n}\right) & n\ even \end{cases} \tag{6.4}$$

being

$$\beta = \ln\left[\coth\left(\frac{L_{ar}}{17.37}\right)\right], \qquad \gamma = senh\left(\frac{\beta}{2n}\right)$$

The next step is to obtain the bandpass prototype with ideal admittance inverters and distributed resonators. The theory behind this process is not included, as the aim of this chapter is not to describe the design process of a parallel-coupled lines filter, but rather to use this topology in order to achieve an ultra-wideband response using stepped impedance resonators. However, the complete development can be found in [9].

Starting from the normalized lowpass prototype, the transformation into a prototype with all shunt capacitors using admittance inverters is carried out. Subsequently, impedance and admittance scaling is applied, followed by the corresponding frequency transformation. Finally, lumped resonators are substituted by distributed resonators, which are the transmission lines. This yields the following design equations:

$$\frac{J_{01}}{Y_0} = \sqrt{\frac{\pi}{2} \cdot \frac{FBW}{g_0 \cdot g_1}} \quad ; \quad \frac{J_{n,n+1}}{Y_0} = \sqrt{\frac{\pi}{2} \cdot \frac{FBW}{g_n \cdot g_{n+1}}}$$

$$\frac{J_{j,j+1}}{Y_0} = \frac{1}{\sqrt{g_j g_{j+1}}} \cdot \frac{\pi \cdot FBW}{2} \qquad j = 1 \quad to \quad n-1 \tag{6.5}$$

where $FBW = \frac{f_2 - f_1}{f_0}$ is the fractional bandwidth.

After obtaining the bandpass prototype with ideal admittance inverters and distributed resonators, the even-mode and odd-mode characteristic impedances of the coupled sections (Z_{0_e} and Z_{0_o}) equivalent to the inverters are calculated. These values are given by

$$\begin{aligned} \left(Z_{0_e}\right)_{j,j+1} &= \frac{1}{Y_0}\left[1 + \frac{J_{j,j+1}}{Y_0} + \left(\frac{J_{j,j+1}}{Y_0}\right)^2\right], \qquad j = 0,1,\dots,n \\ \left(Z_{0_o}\right)_{j,j+1} &= \frac{1}{Y_0}\left[1 - \frac{J_{j,j+1}}{Y_0} + \left(\frac{J_{j,j+1}}{Y_0}\right)^2\right], \qquad j = 0,1,\dots,n \end{aligned} \tag{6.6}$$

The following is the calculation of the impedance ratio K of the SIRs. Using Eqs. (4.6), (4.7) and (4.9), it can be defined the separation between the first and the third resonance of a triple-mode SIR, normalized to the central resonance frequency (f_2):

$$\Delta f_{13} = \frac{f_3 - f_1}{f_2} = \frac{2}{\pi} \cdot 2\tan^{-1}(\sqrt{K}) \tag{6.7}$$

This relationship has been plotted in MATLAB, resulting in Figure 6.1.

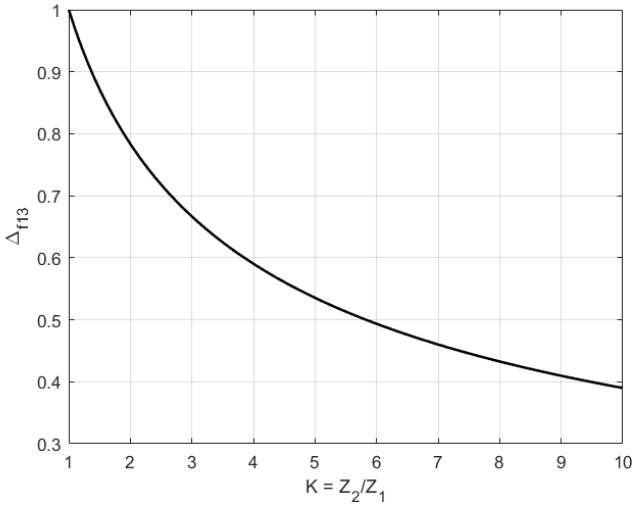

Figure 6.1. Relationship between impedance ratio and normalized frequency separation in a triple-mode SIR.

For this purpose, it is necessary to obtain the transmission poles frequencies normalized to the central frequency using the following expression:

$$f_{p_k} = \frac{FBW \cdot \Omega_k}{2} + 1 \quad for\ k = 1,2,\dots,n \tag{6.8}$$

where Ω_k is given by Eq. (6.3).

In this case, since an eight-order filter with no transmission pole at the central frequency is going to be designed, it is defined

$$\Delta f_{13} = f_a - f_b \tag{6.9}$$

with

$$f_a = \frac{f_{p_2} + f_{p_3}}{2} \tag{6.10}$$

$$f_b = \frac{f_{p_6} + f_{p_7}}{2} \tag{6.11}$$

On the other hand, by setting the width W_2 to the minimum manifacturable dimension, the characteristic impedance of the high-impedance section Z_2 is obtained using Eq. (5.1), and after calculating Δf_{13} and determining the corresponding value of K from the previous figure, Z_1 is obtained as:

$$Z_1 = Z_2/R$$

Finally, having obtained all the necessary parameters for the design, the schematic of the filter with ideal transmission lines is presented in Figure 6.2, which consists of two identical resonators coupled with impedance steps coupled in parallel. The coupled sections have an electrical length of 90° at the central frequency, while the low-impedance sections have an electrical length of 180°.

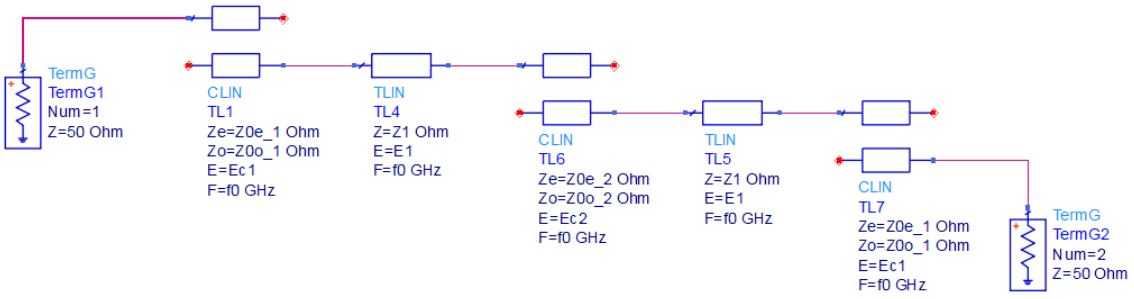

Figure 6.2. Schematic with ideal lines of parallel coupled-line filters with stepped impedance resonators.

This process will be followed to carry out the design in the subsequent section.

6.2. FILTER DESIGN

The design of an eighth-order parallel-coupled line filter with two triple-mode SIRs in microstrip technology is proposed. Ideally, the filter will have a central frequency of $f_c = 5.5\ GHz$ and a fractional bandwidth of $BW_{\%} = 90.91$. The design aims to match a Chebyshev response with a return loss level in the passband set at 15 dB, following the method described in the previous section.

Initially, the same dielectric material, Rogers RO4350B, will be used, whose characteristics are shown in Figure 5.1.

From the specified return loss value and its definition, given in Eq. (2.5), it is obtained

$$|s_{11}|^2 = 10^{-\frac{RL}{10}} = 10^{-\frac{15}{10}} = 0.3162$$

Since a filter is ideally a lossless network, its scattering matrix must satisfy the unitarity theorem:

$$(S^T)^* \cdot S = I \tag{6.12}$$

Therefore, it must be satisfied

$$|s_{21}|^2 + |s_{11}|^2 = 1 \tag{6.13}$$

From this, the value of the parameter s_{21} can be derived, and consequently, the ripple constant of the filter:

$$L_{ar} = -10\log_{10}|s_{21}|^2 = 0.1396\ dB$$

Using this, the normalized elements are calculated from Eq. (6.4), and their values are presented in Table 6.1.

g_0	g_1	g_2	g_3	g_4	g_5	g_6	g_7	g_8	g_9
1.0000	1.2747	1.4163	2.1975	1.5671	2.2450	1.5339	2.0290	0.8898	1.4326

Table 6.1. Values of the LC elements of the normalized lowpass prototype.

Using Eqs. (6.5) and (6.6), it is obtained

$$J_{0,1} = J_{8,9} = 1.0584 \qquad \left(Z_{0_e}\right)_{0,1} = \left(Z_{0_e}\right)_{8,9} = 158.93 \qquad \left(Z_{0_o}\right)_{0,1} = \left(Z_{0_o}\right)_{8,9} = 53.092$$

which are the values of the even-mode and odd-mode characteristic impedances of the coupled lines, corresponding to the input and output (I/O) coupling, being $FBW = 0.9091$, $Y_0 = 1/Z_0$, y $Z_0 = 50\ \Omega$.

As explained in the previous section, the next step is to calculate the impedance ratio, for which it is necessary to obtain the frequencies of the transmission poles normalized to the central frequency, given by Eq. (6.8). The obtained values are presented in Table 6.2:

k	1	2	3	4	5	6	7	8
$f_p(k)/f_0$	1.4458	1.3779	1.2525	1.0887	0.9113	0.7475	0.6221	0.5542

Table 6.2. Theoretical frequencies of the transmission poles of the 8th order Chebyshev UWB filter with two triple-mode SIRs normalized to the center frequency.

Applying Eqs. (6.10) and (6.11), it is calculated

$$\Delta f_{13} = 0.6304$$

and from Figure 6.1 it is obtained

$$K = Z_2/Z_1 = 3.43$$

As in the previous design, the minimum dimension must be of $0.25\ mm$ due to the available fabrication technology. Therefore, this value is set for the width of the high-impedance section (W_2), which corresponds to a characteristic impedance of $Z_2 = 116\ \Omega$ using the aforementioned substrate, as shown in Figure 5.2.

With this, it is calculated

$$Z_1 = Z_2/K = 33.82\ \Omega$$

Having obtained all the necessary parameters, a circuit-level simulation with ideal transmission lines is carried out using ADS software, by substituting these values into the schematic shown in Figure 6.2. The values of the even- and odd-mode impedances are initially set to the same value as those previously calculated for the I/O coupling. These values, along with all other design variables, were then tuned through optimization.

The resulting response is shown below in Figure 6.3.

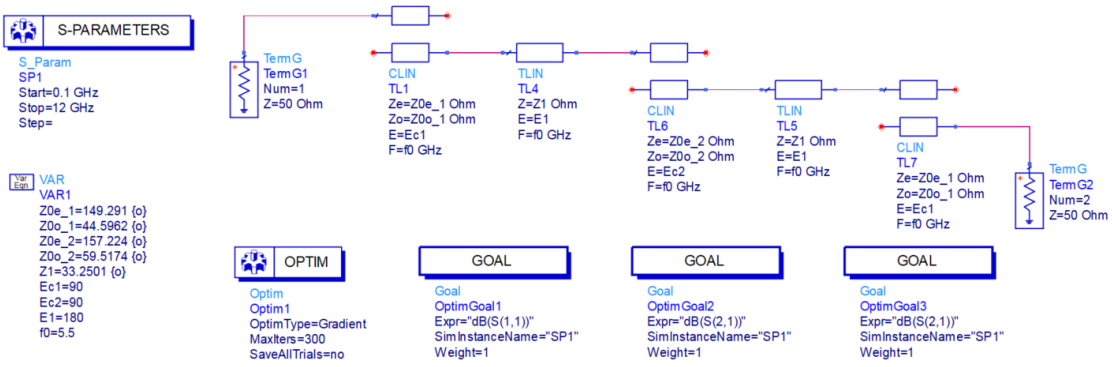

Figure 6.3. Schematic of 8th order Chebyshev UWB filter with two triple-mode SIRs.

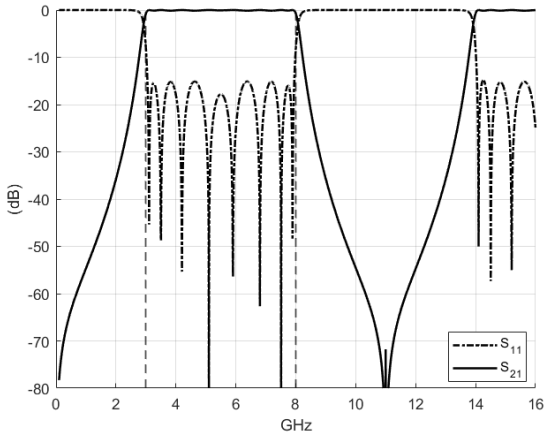

(a)

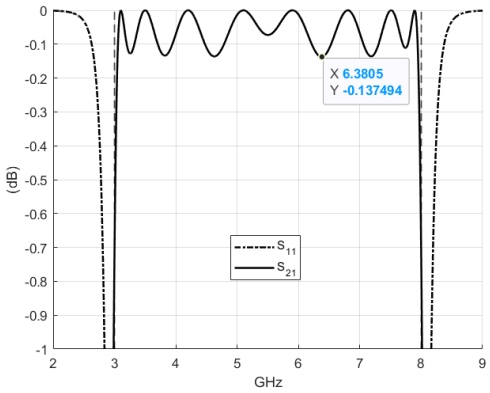

(b)

Figure 6.4. Circuit simulation results with ideal lines of 8th order Chebyshev UWB filter with two triple-mode SIRs. (a) S-parameters. (b) Insertion loss level.

As can be seen in Figure 6.4, the ideal response shows an ultra-wideband behaviour with the abovementioned specifications. It is interesting to observe that the spurious passband appears approximately at $16.5\ GHz \approx 3 \cdot f_0$, much farther from the main band than in the previous design.

Furthermore, it has been achieved a similar response to the theoretical one resulting from the Chebyshev approximation. This is depicted in Table 6.3, which compares the theoretical transmission pole frequencies with those obtained from the simulation.

	k	1	2	3	4	5	6	7	8
Theoretical	$f_p(k)$ $[GHz]$	3.048	3.421	4.111	5.012	5.988	6.889	7.579	7.952
Simulated	$f_p(k)$ $[GHz]$	3.093	3.497	4.204	5.122	5.883	6.794	7.502	7.906

Table 6.3. Theoretical vs. simulated frequencies of the transmission poles of the 8th order Chebyshev UWB with two triple-mode SIRs filter using ideal lines.

The subsequent step is to obtain the circuit response with real transmission lines, for which the following schematic has been created, illustrated in Figure 6.5.

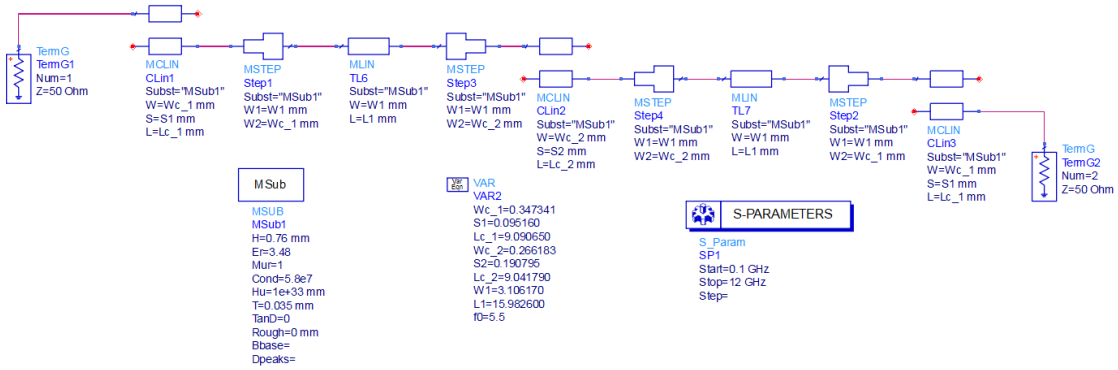

Figure 6.5. Schematic of the 8th order Chebyshev UWB filter with two triple-mode SIRs using real lines.

As it can be observed, the pretended dimensions for realizing the required couplings are below the limit of $0.25\ mm$, in accordance with the available manufacturing technology. Therefore, the design variables have been optimized in an attempt to achieve a reasonable response while complying with this constraint, but no improvement over the response shown in the following figure has been obtained.

In Figure 6.6 it is clearly visible that for both the input and output couplings, particularly for the first one, a smaller separation between those sections is needed to improve the response, as was previously demonstrated in Figure 5.5.

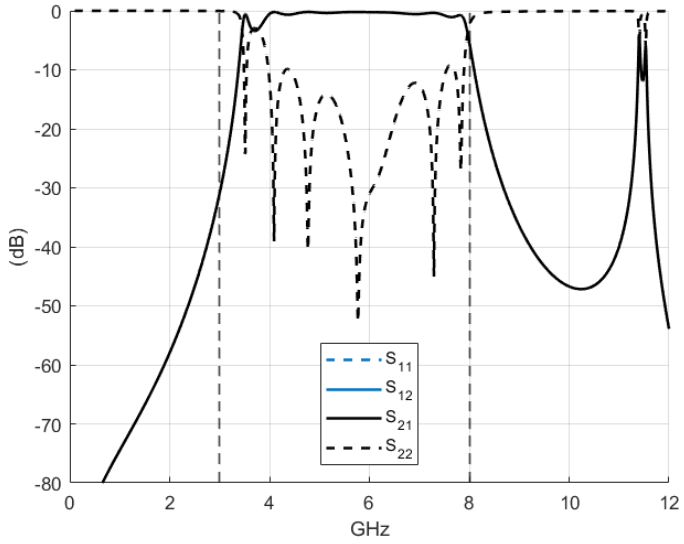

Figure 6.6. Circuit response of the 8th order Chebyshev UWB filter with two triple-mode SIRs using real lines.

To address this issue, which was also encountered in the previous design, several possibilities have been considered, such as reducing the design bandwidth or relaxing the required return loss level. Efforts were also directed towards increasing the I/O coupling by introducing interdigital-coupled feed lines, analyzed in Section 4.5. However, this approach has only increased the design complexity and the number of design parameters, without leading to any noticeable improvement.

Additionally, an attempt has been made to implement the same ideal response with three SIRs, but no significant improvement has been achieved. This outcome was expected, since increasing the number of resonators requires stronger coupling, and since the design is limited by a minimum separation, the response deteriorates.

Therefore, it has been ultimately decided to change the substrate. When using a substrate with higher relative permittivity, the line spacing must be increased to achieve the same coupling level, or equivalently, maintaining the same separation results in stronger coupling. However, it also implies narrower lines for the same characteristic impedance level given the relationship between W y ε_r, shown in section 5.1. This is also affected by the thickness of the dielectric, so it must be considered.

After several evaluations the Rogers RO3006 substrate has been finally selected, with a thickness of $1.27mm$ and a conductor with a thickness of $35\mu m$. The provided relative permittivity of the substrate by the manufacturer is 6.15 ± 0.15, and the loss tangent at $10\ GHz$ is 0.0022, as depicted in Figure 6.7.

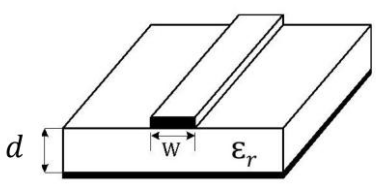

$$d = 1.27\ mm$$

$$\varepsilon_r = 6.15$$

$$tan\delta = 2.2 \cdot 10^{-3}$$

Figure 6.7. Microstrip line technology for the fabrication of the 8th order Chebyshev UWB filter with two triple-mode SIRs [26].

With this change, the design procedure has been carried out again.

The values of the lumped elements and the transmission pole frequencies remain unchanged, and so does the impedance ratio, as these parameters do not depend on the material used. The same applies to the theoretical values of the even-mode and odd-mode characteristic impedances of the parallel-coupled lines.

What does change is the real value of the characteristic impedances for a given width. Now, by setting $W_2 = 0.25\ mm$, a value of $Z_2 = 107.86\ \Omega$ for the high-impedance section, which implies

$$Z_1 = Z_2/K = 31.45\ \Omega$$

Following this, as done previously, the model with ideal lines is obtained. Figure 6.8 represents the schematic and the result after circuit optimization of the design variables.

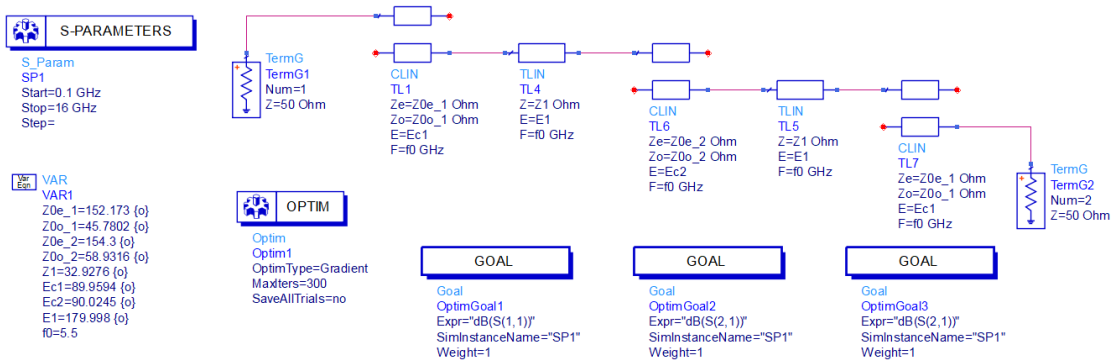

(a)

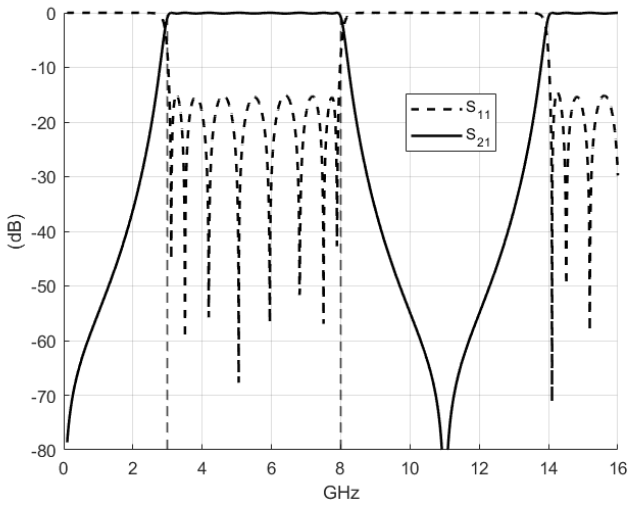

(b)

Figure 6.8. (a) Schematic and (b) circuit response of the 8th order Chebyshev UWB filter with two triple-mode SIRs using ideal lines for the new dielectric material.

It is evident that the circuit response with ideal transmission lines is very similar to that of the initial design.

Table 6.4 presents a comparison between the transmission pole frequencies of the simulation and the theoretical ones. In this case, closer values have been achieved, resulting in a more accurately approximation to the desired performance.

	k	1	2	3	4	5	6	7	8
Theoretical	$f_p(k)$ $[GHz]$	3.048	3.421	4.111	5.012	5.988	6.889	7.579	7.952
Simulated	$f_p(k)$ $[GHz]$	3.105	3.503	4.188	5.050	5.949	6.818	7.502	7.894

Table 6.4. Theoretical vs. simulated frequencies of the transmission poles of the 8th order Chebyshev UWB filter with two triple-mode SIRs using ideal lines for the new dielectric material.

The subsequent stage involves the simulation with real transmission lines. Figure 6.9 shows the new schematic, and Figure 6.10 shows the circuit results including dielectric losses.

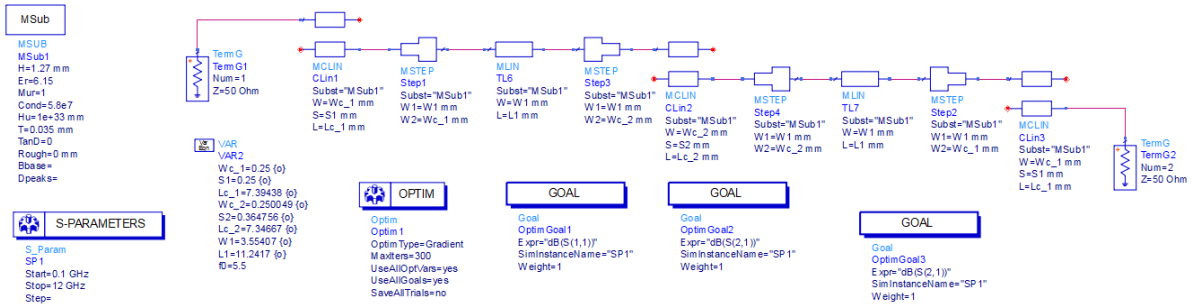

Figure 6.9. Schematic of the 8th order Chebyshev UWB filter with two triple-mode SIRs using real lines for the new dielectric material.

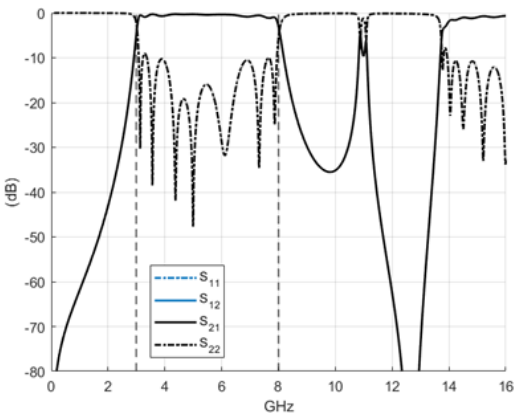

(a)

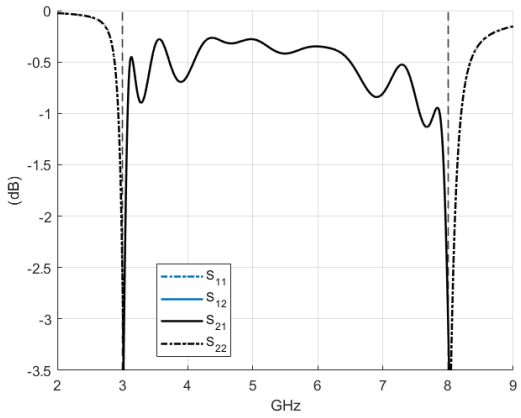

(b)

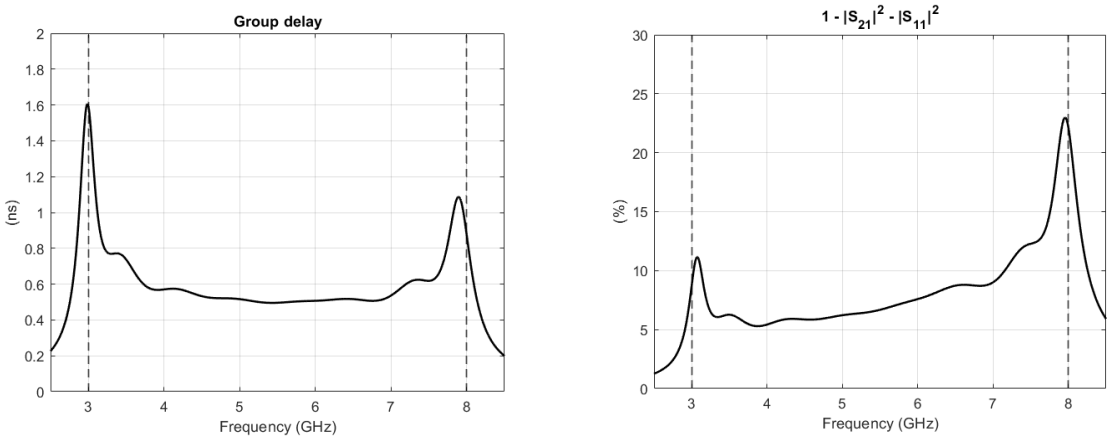

(c) (d)

Figure 6.10. Circuit simulation results of 8th order Chebyshev UWB filter with two triple-mode SIRs. (a) S-parameters. (b) Insertion loss level. (c) Group delay. (d) Power balance.

As depicted in the previous figure, an ultra-wideband response has been achieved, with a passband between 3 GHz and 8 GHz. In this frequency range, return loss level is better than 9 dB, and insertion losses maintain below 1.2 dB.

The group delay variation within the band of interest is less than 1.2 ns, and the losses reach up to 24% of the total power.

If those values are compared to the ones of the design of the previous chapter, it can be noticed that, despite a degradation in return loss and the increased variation in group delay and total losses, a significant increase in bandwidth has been achieved without excessively compromising the response. Furthermore, both the loss level and the return loss would improve substantially if high-temperature superconducting technology were employed, resulting in significantly better performance with this topology compared to that obtained with a single triple-mode SIR.

6.3. ELECTROMAGNETIC MODELLING AND SIMULATION OF THE FILTER

The next step is the electromagnetic simulation of the filter. Once again, Ansys HFSS software has been used, along with the automation tools employed throughout the project.

The 3D model of the structure is depicted in Figure 6.11.

The defined configuration is the same as in the design of the previous chapter, except that in this case lumped ports were chosen to streamline the optimization process, which also requires adding simulation volume along the X-axis. This also enables the verification of the accuracy level of the results obtained with this type of port by comparing them with subsequent measurements.

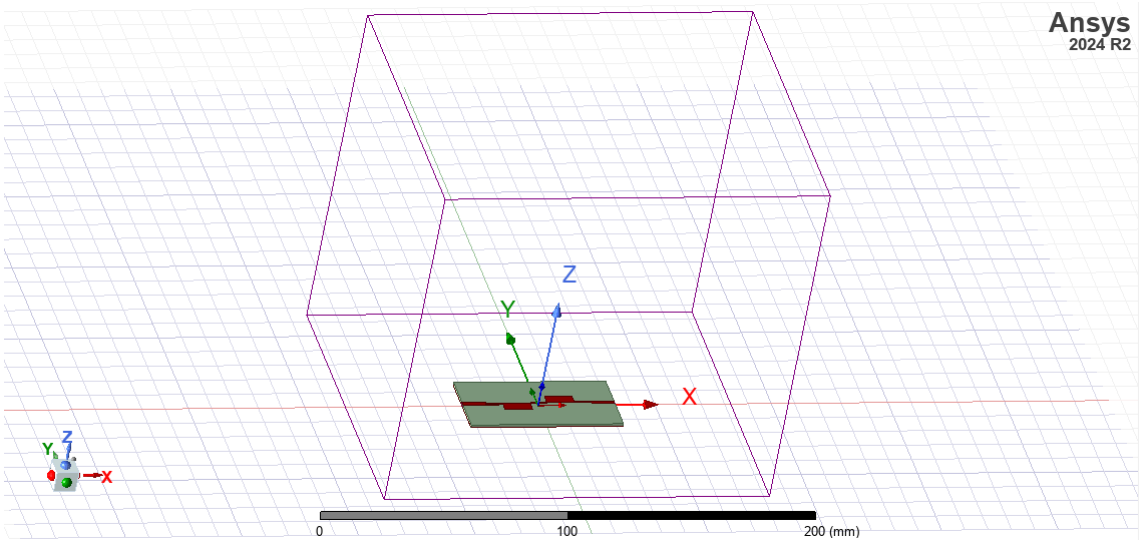

Figure 6.11. Electromagnetic model of 8th order Chebyshev UWB filter with two triple-mode SIRs.

The electromagnetic performance, presented in Figure 6.12, does not meet the desired objectives. Therefore, it has been necessary to perform an electromagnetic optimization of the structure. Part of this process is shown in Figure 6.13.

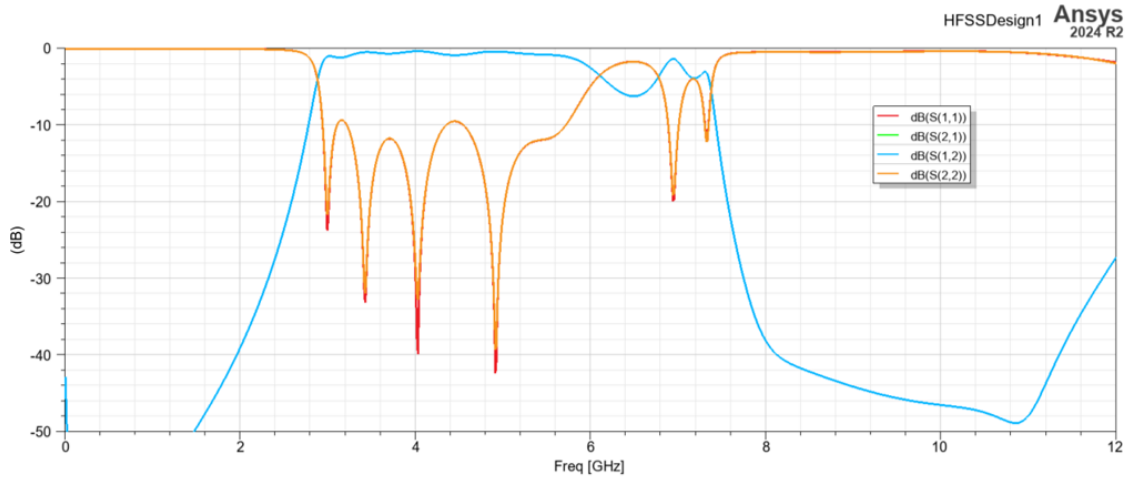

Figure 6.12. Electromagnetic simulation result of 8th order Chebyshev UWB filter with two triple-mode SIRs.

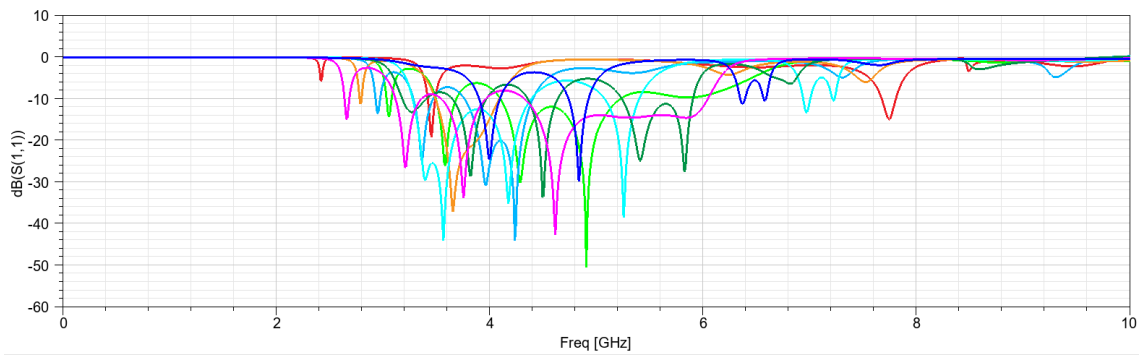

(a)

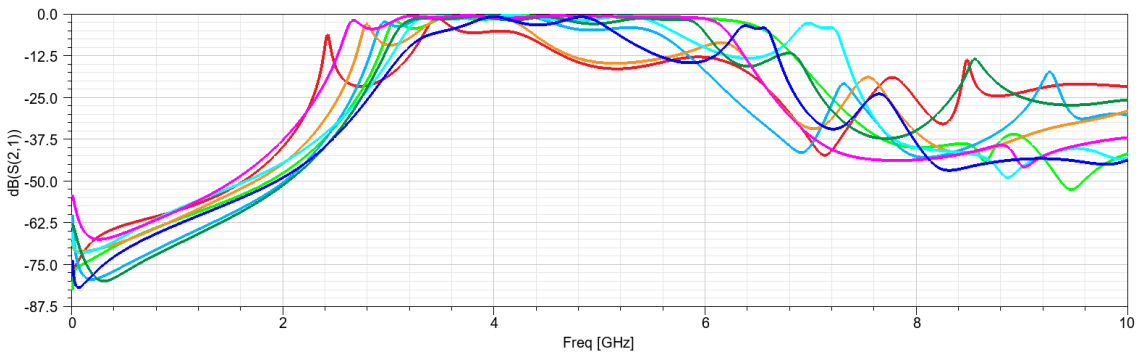

(b)

Figure 6.13. Electromagnetic optimization process of 8th order Chebyshev UWB filter with two triple-mode SIRs. (a) S11 and (b) S21.

This procedure has involved, not only the optimization of the design variables, but also modifications to the filter layout to achieve the desired coupling level. After several iterations, the coupled section between the resonators has been slightly reduced, and the I/O coupling has been increased by arranging the resonators as illustrated in the following figure.

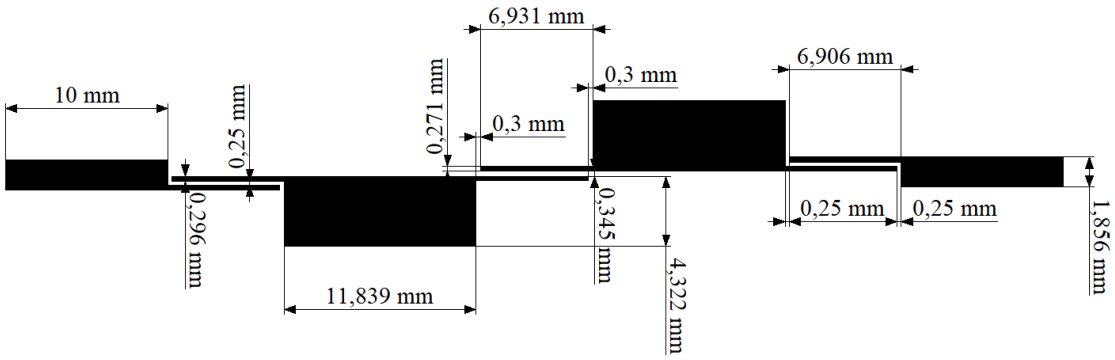

Figure 6.14. Layout of 8th-order Chebyshev UWB filter with two triple-mode SIRs.

Figure 6.14 shows the filter layout. When comparing it to Figure 5.11 it can be noticed that this design is slightly less compact than the one of the previous chapter, as reflected in Table 6.5.

It is important to note that these dimensions would be considerably smaller if a more sophisticated fabrication technology were available.

	Total length (mm)	*Total width (mm)*
SIR type II UWB filter	56.397	6.291
8th − order Chebyshev UWB filter	65.221	8.990

Table 6.5. Comparison of the dimensions of the type-II SIR UWB filter and the 8th-order Chebyshev UWB filter with two triple-mode SIRs.

By examining the previous figure, it can be noticed that several lines and widths are at the lower limit imposed. This indicates that the performance has once again been compromised by this constraint. In fact, changing the dielectric material alone has been insufficient, and it has been necessary to significantly reduce the design bandwidth, as reflected in Figure 6.15, in which the electromagnetic simulation results are compared to the circuit response.

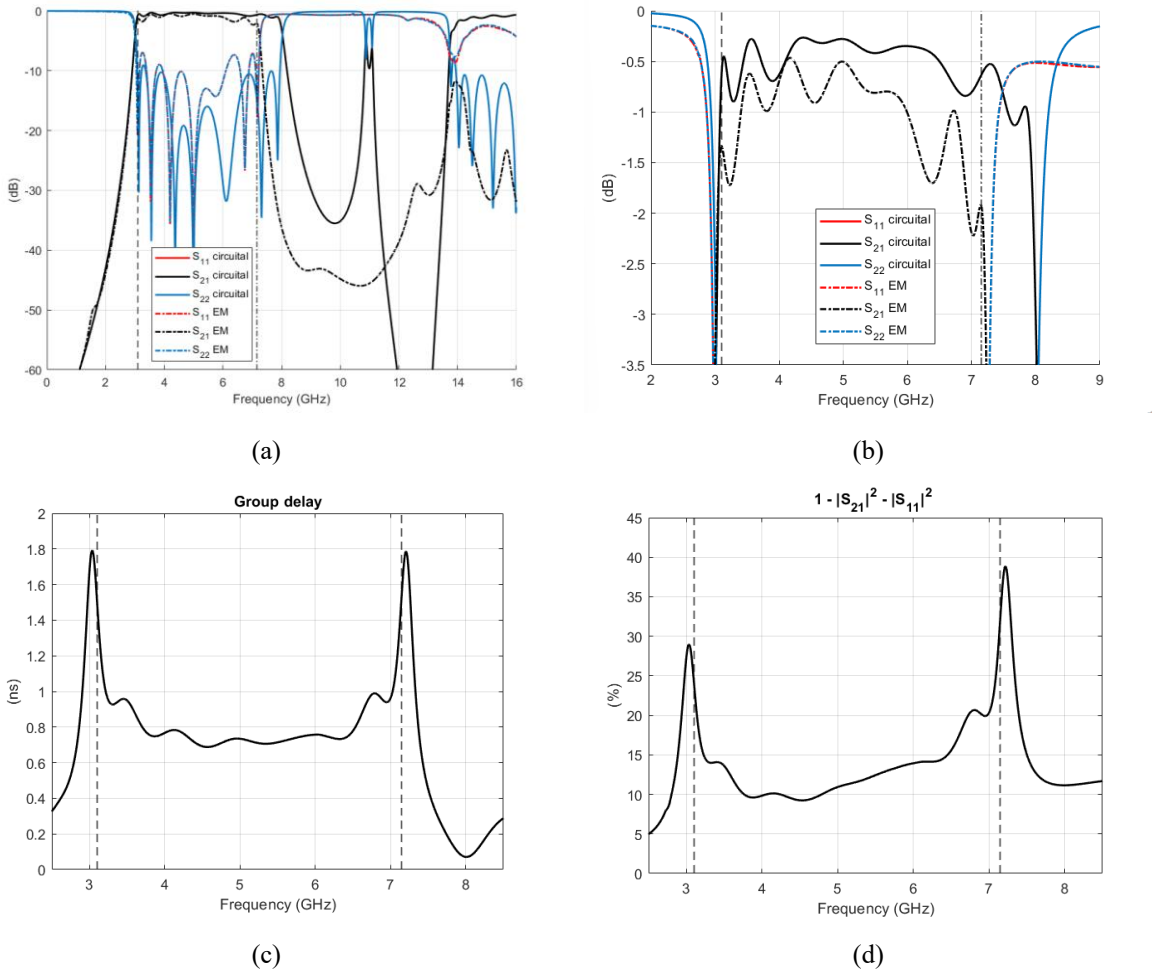

Figure 6.15. Electromagnetic simulation results after EM optimization of 8th order Chebyshev UWB filter with two triple-mode SIRs. (a) S-parameters: circuit vs. EM. (b) Insertion loss level: circuit vs. EM. (c) Group delay. (d) Power balance.

These figures clearly illustrate the bandwidth reduction, from a passband between 3 GHz and 8 GHz in the circuit-level simulation to a final passband between 3.1 GHz and 7.15 GHz in the electromagnetic response.

Nevertheless, the spurious response previously present at 11 GHz has been successfully shifted to 14 GHz.

6.4. FILTER FABRICATION

Although the result is not as optimal as initially desired, it is considered acceptable to proceed with the filter fabrication. This stage is particularly relevant, as it will enable the analysis of the accuracy of the simulation results.

The procedure followed for the fabrication is the same as in the previous chapter.

Figure 6.16. Fabricated 8th order Chebyshev UWB filter with two triple-mode SIRs.

In this case, no manufacturing defects are observed in the fabricated prototype, shown in Figure 6.16.

6.5. FILTER MEASUREMENT

As in the previous design, the last step is the filter measurement with the VNA. The system has been calibrated up to 20 GHz, and the configuration used in this process is depicted in Figure 6.17.

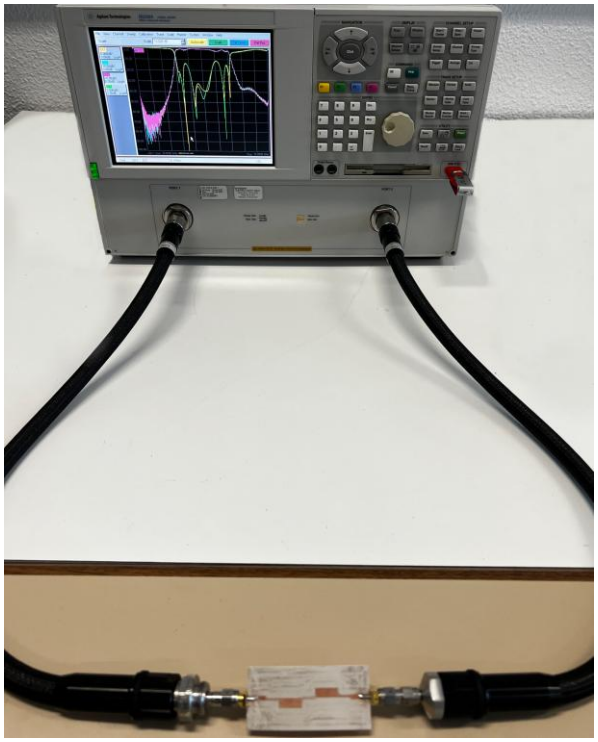

Figure 6.17. Measurement setup of 8th order Chebyshev UWB filter with two triple-mode SIRs.

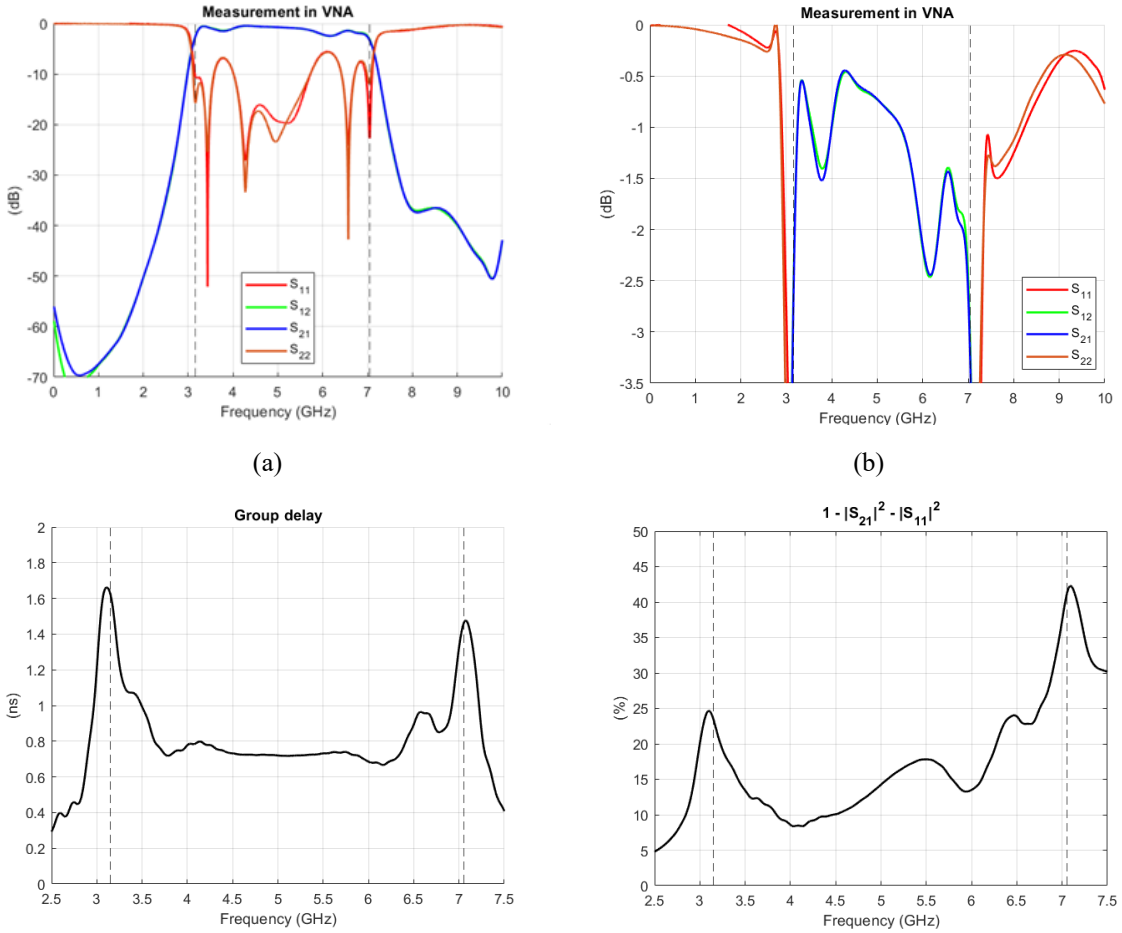

Figure 6.18. Measurement results of 8th order Chebyshev UWB filter with two triple-mode SIRs. (a) S-parameters. (b) Insertion loss level. (c) Group delay. (d) Power balance.

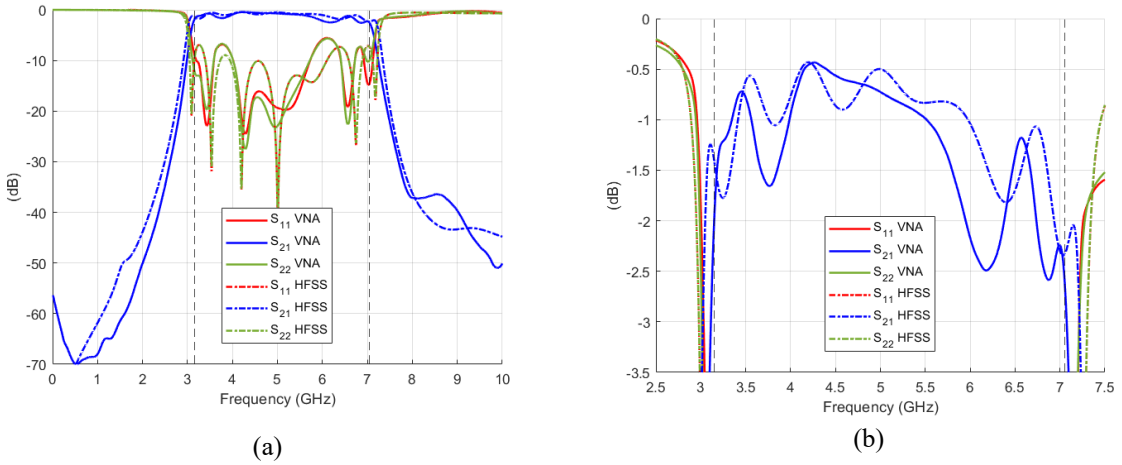

Figure 6.19. Comparison between measurement results and EM simulation results of 8th order Chebyshev UWB filter with two triple-mode SIRs. (a) S-parameters. (b) Insertion loss level.

Figure 6.18 shows the obtained measurements, and Figure 6.19 the comparison with the electromagnetic simulation. As observed, both results are significantly similar, which means that a sufficiently accurate simulation has been achieved.

Finally, a filter with a bandwidth ranging from 3.15 GHz and 7.05 GHz has been achieved, with a center frequency of 5.1 GHz, which corresponds to a fractional bandwidth of 76.47%. The measurements show that the insertion losses have increased up to 2.5 dB within the band of interest, while the return losses have deteriorated to 5.7 dB.

Regarding the group delay, the filter presents a variation lower than 1 ns in the passband, in addition to losses that have risen to 44% of the total power.

Once again, it is essential to emphasize that this performance is significantly limited by the employed technology, and that using HTS technology would yield a significantly better result, as demonstrated throughout the project.

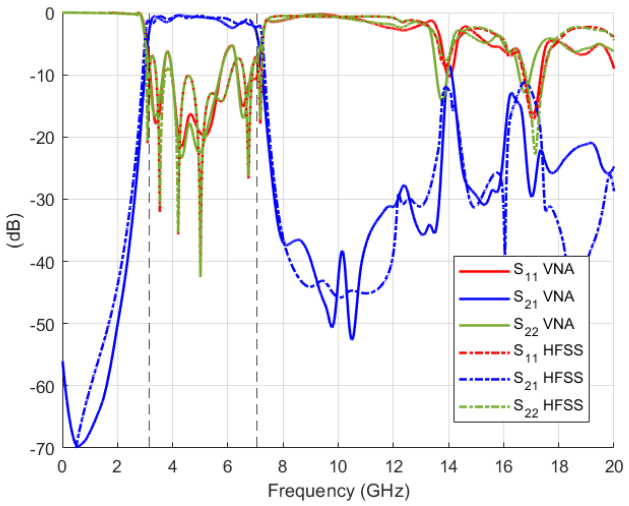

Figure 6.20. Far rejection of 8th order Chebyshev UWB filter with two triple-mode SIRs. Measurement results vs. EM simulation.

As in the previous chapter, it is interesting to identify the appearance of the spurious band, which in this case is located around 14 GHz, corresponding approximately to $2.75 \cdot f_0$. This can be seen in Figure 6.20

6.6. CONCLUSIONS

In this chapter, an eight-pole Chebyshev ultra-wideband filter with two triple mode stepped impedance resonators has been designed, fabricated, and measured.

As in the previous design, the filter performance has been limited by the available materials and the employed technology. Nevertheless, an ultra-wideband filter has been successfully developed, achieving the results presented below in Table 6.6.

BW	f_0	$BW_{\%}$	IL_{max}	RL_{min}	$Delay\ variation$	$Total\ losses$
$3.15\ GHz\ -\ 7.05\ GHz$	$5.1\ GHz$	76.47%	$2.5\ dB$	$5.7\ dB$	$< 1\ ns$	$< 44\%$

Table 6.6. Final results of 8th order Chebyshev UWB filter with two triple-mode SIRs.

Comparing these results with the ones in Table 5.1, it is evident that the second topology outperforms the previous one in terms of bandwidth.

In addition, the simulation using lumped ports has also been successfully validated, and the filter design process has contributed to refining both the automation scripts and the electromagnetic optimization stage.

Therefore, it can be concluded that this chapter accomplishes the established objectives.

CHAPTER SEVEN

Conclusions and Future Work

7.1. CONCLUSIONS

Once the proposed stages for the development of this project are completed, the main conclusions can be drawn.

First, different topologies for ultra-wideband filters have been studied through the design of a filter based on cascaded filtering stages and a composite filter. These structures have been developed with high-temperature superconducting materials, which have allowed to evaluate the results that can be achieved with this technology, not only in terms of performance but also regarding size. The obtained responses are remarkably good considering the simplicity of these topologies, with a passband between $3.1\ GHz$ and $10.6\ GHz$, thus meeting the spectral range established for UWB communications.

Subsequently, it has been studied a high-temperature superconducting stub-loaded multi-mode resonator ultra-wideband filter, designed in [24]. Efforts have been made to improve the results provided by the authors, which has been not possible due to the high complexity of the filter, Nevertheless, this process has contributed to understanding and consolidating the fundamentals and various design strategies for ultra-wideband filters using HTS technology, thereby fulfilling one of the project's main objectives.

Regarding the final designs, the use of HTS technology has been unfeasible, so conventional materials and in-house manufacturing have been used instead.

First, a triple-mode stepped impedance resonator ultra-wideband filter has been successfully designed, fabricated and measured despite challenges encountered due to the simplicity of the available technology. To achieve this, it has been necessary to push the fabrication limits of certain line dimensions and even changing the type of resonator employed. Moreover, a manufacturing error altered the filter's performance. Despite this, a filter with a center frequency of $f_0 = 4.35\ GHz$ and a fractional bandwidth of $BW_{\%} = 62.07\%$ has been obtained, achieving relatively good performance considering the used materials, thus satisfactorily meeting the objectives of the corresponding chapter.

On the other hand, the eight-pole Chebyshev ultra-wideband prototype with two triple-mode stepped impedance resonators has also been designed and implemented adequately. Similar difficulties have arisen in this case, driven by the same technological limitations as before. These have been addressed by forcing the filter parameters, relaxing the requirements, changing the employed material and modifying the layout of the structure. This process has helped consolidate many of the concepts explored throughout the project. Furthermore, it has been achieved a wider bandwidth than in the previous filter, with a response centered at $f_0 = 5.1\ GHz$ and a fractional bandwidth of $BW_{\%} = 76.47\%$.

With these two designs, not only the complete cycle of design, fabrication, and measurement of a radiofrequency filter has been successfully completed, but also it has been possible to compare the performance and dimensions of structures made with conventional materials to those using HTS technology, thus fulfilling the project's primary objective.

Additionally, MATLAB automation scripts have been developed and refined throughout the project, which has greatly accelerated the design and optimization electromagnetic optimization processes for filters in the Ansys HFSS software. Furthermore, convergence and result accuracy studies have been satisfactorily completed for all electromagnetic designs, verifying the correct definition on simulation ports, radiation box, and meshing to obtain accurate results while reducing simulation time. This has also fulfilled the secondary objectives defined at the beginning of the project.

7.2. FUTURE WORK

As highlighted in various sections of the project, the designs have been constrained by several limitations, which adds merit to the achieved results while leaving significant room for improvement.

One of the main challenges has been the unavailability of HTS material for fabrication. Employing such materials would enable improved results with better return loss level, higher out-of-band rejection and a more compact structure. Since these materials and its implementation methods are not accessible at the Department of Signals, Systems and Radiocommunications (SSR), outsourcing the manufacturing process could be considered. It would entail an additional cost but also have a significant impact in terms of research value and project improvement.

However, given the complexity of this proposal, significant improvements could also be achieved by changing only the fabrication technology. In this project, a micro-milling machine has been used, which requires minimum dimensions to prevent the milling tool from overlapping the filter's contour lines, greatly limiting the design process. By employing some other methods, such as laser technology, more compact structures could be fabricated, enabling higher coupling levels and, consequently, a significantly improved response.

Future work with less impact involves the initial designs. In them, filtering stages were combined to achieve an ultra-wideband response. By refining and developing more complex individual filters, particularly the highpass section, better performance could be achieved, primarily in terms of selectivity. Additionally, these designs could be electromagnetically optimized to validate the results obtained from circuit simulations and, if feasible, they could then be fabricated and measured to complete the analysis of the corresponding topologies.

Finally, regarding the study on accuracy and simulation efficiency, a comparison could be conducted among different electromagnetic simulation softwares currently available for the designs developed. This analysis could compare the Frequency Domain Solver and the Multilayer Solver of CST Studio Suite, and Momentum Microwave of ADS, in addition to the Ansys HFSS software used in this project. This would allow not only a comparison of the fluency and accuracy of each tool but also provide a broader validation stage before fabrication.

References

[1] BOE-A-2020-8286, (2020). Retrieved from https://www.boe.es/eli/es/o/2020/07/13/etd666 [Accessed: May. 10, 2025].

[2] Official Journal of the European Union. (2024). *Commission implementing decision (EU) 2024/1467*. Retrieved from: https://eur-lex.europa.eu/legal-content/EN/TXT/PDF/?uri=OJ%3AL_202401467. [Accessed: May. 11, 2025].

[3] Qorvo US, Inc. (2021). *Getting back to basics with ultra-wideband (UWB)*. Retrieved from: https://www.qorvo.com/resources/d/qorvo-getting-back-to-basics-with-ultra-wideband-uwb-white-paper. [Accessed: May. 11, 2025].

[4] Chávez-Santiago, R., Balasingham, I., Bergsland, J. and Chiu, H.-C., 2012. Ultrawideband Technology in Medicine: A Survey. *Journal of Electrical and Computer Engineering*, vol. 2012, no. 1, ISSN 2090-0147. DOI 10.1155/2012/716973.

[5] European VLBI Network. (2022). *The European VLBI network*. Retrieved from: https://evlbi.org/. [Accessed: May. 11, 2025].

[6] Radcliffe, J.F., Mckean, J.P., Herbé-George, C., Coetzer, L. and Matsepane, T., 2025. *Latest developments in wide-field VLBI*., DOI 10.48550/arxiv.2504.19579.

[7] Hong, J.-S. and Wiley Online Library, 2011. *Microstrip filters for RF/microwave applications*. 2nd ed. Hoboken, N.J.: Wiley. ISBN 9786613813466.

[8] J. R. Montejo Garai, *Teaching material for the course Analysis and Design of Circuits.* Department of Signals, Systems and Radiocommunications, ETSI Telecomunicación UPM.

[9] García Amorós, G. and Montejo Garai, J.R., 2024. *Diseño e implementación en tecnología planar de filtros con respuesta máximamente plana en retardo de grupo para sistemas de comunicaciones 5G*. S.l.: E.T.S.I. Telecomunicación (UPM).

[10] Pozar, D.M., 2012. *Microwave engineering*. 4th ed. Hoboken, NJ: John Wiley & Sons. ISBN 978-0-470-63155-3.

[11] Schmidy, V.V., Müller, P. and Ustinov, A.V., 1997. *The Physics of Superconductors: Introduction to Fundamentals and Applications*. 1st ed. S.l.: s.n. ISBN 3-662-03501-4.

[12] Qiu, X., 2011. *High-temperature superconductors*. 1st edition. S.l.: s.n. ISBN 9780857091031.

[13] *Teaching material for the course Radiofrequency Optimization Techniques.* Department of Signals, Systems and Radiocommunications, ETSI Telecomunicación UPM.

[14] Cameron, R.J., Kudsia, C.M. and Mansour, R.R., 2018. *Microwave filters for communication systems: fundamentals, design, and applications*. 2nd ed. Hoboken, New Jersey: Wiley. ISBN 1-119-29238-7.

[15] Microsoft (June 2021). *The component object model (COM)*. Retrieved from: https://learn.microsoft.com/es-es/windows/win32/com/the-component-object-model [Accessed: Jul. 22, 2025].

[16] Microsoft (June 2023). *[MS-OLEDS]: Object Linking and Embedding (OLE) Data Structures*. Retrieved from: https://learn.microsoft.com/es-es/windows/win32/com/the-component-object-model. [Accessed: Jul. 22, 2025].

[17] Ansys, Inc. (2020). *Ansys HFSS getting started. module 6: HFSS Lumped and Wave Port Basics*. Retrieved from: https://chrome-extension://efaidnbmnnnibpcajpcglclefindmkaj/https://innovationspace.ansys.com/courses/wp-content/uploads/sites/5/2021/07/HFSS_GS_2020R2_EN_LE6_Port_Basics.pdf [Accessed: Jul. 28, 2025].

[18] Ansys, I. (2020). *Ansys HFSS getting started. module 2: Boundaries and simulation space.* Retrieved from: https://chrome-extension://efaidnbmnnnibpcajpcglclefindmkaj/https://innovationspace.ansys.com/courses/wp-content/uploads/2021/07/HFSS_GS_2020R2_EN_LE2_BoundsSimSpace.pdf [Accessed: Jul. 28, 2025].

[19] Shome, P.P., Khan, T., Koul, S.K. and Antar, Y.M.M., 2021. *Two Decades of UWB Filter Technology: Advances and Emerging Challenges in the Design of UWB Bandpass Filters*. IEEE microwave magazine, vol. 22, no. 8, ISSN 1527-3342. DOI 10.1109/MMM.2021.3078040.

[20] Ching-Luh Hsu, Fu-Chieh Hsu and Kuo, J.-K., 2005. *Microstrip bandpass filters for Ultra-Wideband (UWB) wireless communications*. *IEEE MTT-S* International Microwave Symposium Digest, 2005. S.l.: IEEE, pp. 679-682. ISBN 9780780388451. DOI 10.1109/MWSYM.2005.1516698.

[21] Zhu, L., Sun, S., Li, R. and Chang, K., 2012. *Microwave bandpass filters for wideband communications*. 1st ed. Hoboken: John Wiley & Sons. vol. 232. ISBN 9781118197950.

[22] Makimoto, M. and Yamashita, S., 1980. *Bandpass Filters Using Parallel Coupled Stripline Stepped Impedance Resonators*. IEEE transactions on microwave theory and techniques, vol. 28, no. 12, ISSN 0018-9480. DOI 10.1109/TMTT.1980.1130258.

[23] Lei Zhu, Menzel, W., Wu, K. and Boegelsack, F., 2001. *Theoretical characterization and experimental verification of a novel compact broadband microstrip bandpass filter*. APMC 2001. 2001 Asia-Pacific Microwave Conference (Cat. No.01TH8577). S.l.: IEEE, pp. 625-628 vol.2. vol. 2. ISBN 9780780371385. DOI 10.1109/APMC.2001.985451.

[24] Zhou, L, Li H, Long Z, Wu H, Zhang T, Qiao M. *Compact high temperature superconducting multi-mode ultra-wideband filter*. Microw Opt Technol Lett. 2018;1-4. ISSN 0895-2477. DOI 10.1002/mop.31589.

[25] Aebischer, H.A., 2020. *Inductance Formula for Rectangular Planar Spiral Inductors with Rectangular Conductor Cross Section*. Advanced electromagnetics, vol. 9, no. 1, ISSN 2119-0275. DOI 10.7716/aem.v9i1.1346.

[26] *Teaching material for the course Radiofrequency Subsystems.* Department of Signals, Systems and Radiocommunications, ETSI Telecomunicación UPM.

Annex A: Ethical, Economic, Social and Environmental Aspects

A.1 INTRODUCTION

Current communication networks require continuous technological improvement due to their high impact on social, economic, ethical and environmental sectors. Consequently, this impact also extends to radiofrequency filters, whose purpose is to optimally define the operational bandwidth, a valuable and limited resource.

In this section, the impact of this project in the aforementioned areas is briefly outlined.

A.2 DESCRIPTION OF RELEVANT IMPACTS RELATED TO THE PROJECT

Ethical Impact

This project has been oriented toward a positive and transparent impact, addressing ethical considerations related to equitable access to innovation and the responsible use of advances in communications, prioritizing social and environmental benefit over purely commercial interests.

Social Impact

The development of ultra-wideband filters improves the quality and speed of communications, enhancing higher transmission rates and facilitating access to digital services, thus reducing the technological gap. Moreover, due to the multiple applications of UWB technology in medicine, this project also contributed to people's life quality.

Economic Impact

The studied and developed technology increases the efficiency of telecommunications systems, reducing energy losses and optimizing the performance of modern networks. Additionally, frequency band concessions represent one of the largest expenses in current communications systems, so the proper use of the spectrum has a significant economic impact.

Environmental Impact

Devices based on HTS technology consume less energy and generate less heat, thus reducing the carbon footprint and environmental impact of telecommunication infrastructure. Furthermore, this project has been limited to the use of available materials, avoiding additional component production and promoting a more sustainable approach to technological development.

A.3 DETAILED ANALYSIS OF ONE OF THE PRINCIPAL IMPACTS

Despite the project's influence in different areas, much of its relevance lies in the social sphere. Therefore, this section provides a more in-depth analysis of its contributions in this area.

Firstly, in the medical field, the ability of ultra-wideband technologies to transmit high-precision and low-interference signals, as well as low-energy consumption, enables the detection of important diseases. This can significantly help improve people's life expectancy. Moreover, it facilitates faster and simpler diagnoses by enhancing telemedicine systems and remote access to specialized healthcare in isolated regions.

In the military sphere, ultra-wideband filters optimize secure communications, increasing the reliability of critical information transmission, which has a direct impact on people's safety.

On the other hand, UWB technology enables capturing weak signals in a wide frequency range, allowing the detection of cosmic signals and enabling scientific discoveries that expand our understanding of the universe.

All of these applications contribute to technological innovation, generating benefits that positively impact society and the progress of science and technology on a global scale.

A.4 CONCLUSIONS

In this section, the influence of the project on society and the current economy has been reflected, as it represents a significant technological advancement for societal modernization and has a substantial economic impact. Furthermore, it has been developed ethically and responsibly, promoting sustainability through the use of available materials and favouring solutions that add value to the collective environment.

Annex B: Financial Budget

In this section, the total project costs are estimated, considering various expenses involved in its development.

Personnel Costs

Approximately 10 hours per week have been dedicated to this project for 9 months, resulting in a total of 900 hours.

Based on an estimated salary of €17 per hour for a Telecommunications Engineer with a master's degree in radiofrequency technologies, the approximate personnel cost is €15,300.

Software Licensing Costs

MATLAB, Advanced Design System (ADS) and Ansys HFSS have been used for this project.

The academic license for MATLAB costs €262, while Keysight provides free ADS licenses for university students.

On the other hand, the exact cost of the HFSS license is unknown, but it is estimated to be around €5,000.

Thus, the total software cost is approximately €5,262.00.

Material Costs

The total cost of the project also includes the cost of the computer, the manufacturing process, and the instruments used to measure the filters. These are included as depreciation in the following table.

PERSONNEL COSTS	Hours	Hourly cost	Total
	900	17 €	**15,300 €**

MATERIAL RESOURCES COSTS

	Purchase price	Units	Usage (months)	Depreciation (years)	Monthly depreciation	Total
Personal computer	900.00 €	1	9	6	12.5 €	90.00 €
Micro-milling machine (LPKF)	30,000.00 €	1	1	14	178.57 €	178.57 €
Substrate	50.00 €	2	-	-	-	100.00 €
Vector Network Analyzer (VNA)	300,000.00 €	1	1	19	1,315.79 €	1,315.79 €
Calibration kit	8,000.00 €	1	1	19	35.09 €	35.09 €
Coaxial connectors	5 €	4	-	-	-	20.00 €
Coaxial cables	150 €	2	1	5	2.50 €	5.00 €
Soldering machine	1,000.00 €	1	1	11	7.57 €	7.57 €
Total cost of material resources						**1,752.02 €**

SOFTWARE LICENSING COSTS	Licenses	Price	Total
	2	MATLAB 262.00 € HFSS 5,000.00€	**5,262.00 €**

TOTAL BUDGET	**22,314.02 €**

Table B.1. Project budget.